



HAL
open science

Towards a realistic simulation of boreal summer tropical rainfall climatology in state-of-the-art coupled models: role of the background snow-free land albedo

Pascal Terray, K. P. Sooraj, Sébastien Masson, R. P. M. Krishna, Guillaume Samson, A. G. Prajeesh

► To cite this version:

Pascal Terray, K. P. Sooraj, Sébastien Masson, R. P. M. Krishna, Guillaume Samson, et al.. Towards a realistic simulation of boreal summer tropical rainfall climatology in state-of-the-art coupled models: role of the background snow-free land albedo. *Climate Dynamics*, 2018, 10.1007/s00382-017-3812-9 . hal-01630892

HAL Id: hal-01630892

<https://hal.science/hal-01630892>

Submitted on 29 Dec 2017

HAL is a multi-disciplinary open access archive for the deposit and dissemination of scientific research documents, whether they are published or not. The documents may come from teaching and research institutions in France or abroad, or from public or private research centers.

L'archive ouverte pluridisciplinaire **HAL**, est destinée au dépôt et à la diffusion de documents scientifiques de niveau recherche, publiés ou non, émanant des établissements d'enseignement et de recherche français ou étrangers, des laboratoires publics ou privés.

1 Towards a realistic simulation of boreal summer tropical
2 rainfall climatology in state-of-the-art coupled models:
3 Role of the background snow-free land albedo

P. Terray^{1,2,*}, K.P. Sooraj³, S. Masson², R.P.M. Krishna⁴, G. Samson⁵, A.G. Prajeesh³

¹ *Indo-French Cell for Water Sciences, IISc-NIO-IITM-IRD Joint International Laboratory, IITM, Pune, India*

² *Sorbonne Universites (UPMC, Univ Paris 06)-CNRS-IRD-MNHN, LOCEAN Laboratory, 4 place Jussieu, F-75005 Paris, France*

³ *Centre for Climate Change Research, Indian Institute of Tropical Meteorology, Pune, India*

⁴ *Indian Institute of Tropical Meteorology, Pune, India*

⁵ *Mercator Océan, Ramonville-Saint-Agne, France*

Revised for *Climate Dynamics*, 14th July 2017

Corresponding author address: Pascal Terray, Indian Institute of Tropical Meteorology, Pune 411008, India. E-mail: terray@locean-ipsl.upmc.fr

4 **Abstract**

5 State-of-the-art global coupled models used in seasonal prediction systems and climate
6 projections still have important deficiencies in representing the boreal summer tropical
7 rainfall climatology. These errors include prominently a severe dry bias over all the Northern
8 Hemisphere monsoon regions, excessive rainfall over the ocean and an unrealistic double
9 Inter-Tropical Convergence Zone (ITCZ) structure in the tropical Pacific. While these
10 systematic errors can be partly reduced by increasing the horizontal atmospheric resolution of
11 the models, they also illustrate our incomplete understanding of the key mechanisms
12 controlling the position of the ITCZ during boreal summer.

13 Using a large collection of coupled models and dedicated coupled experiments, we show that
14 these tropical rainfall errors are partly associated with insufficient surface thermal forcing and
15 incorrect representation of the surface albedo over the Northern Hemisphere continents.
16 Improving the parameterization of the land albedo in two global coupled models leads to a
17 large reduction of these systematic errors and further demonstrates that the Northern
18 Hemisphere subtropical deserts play a seminal role in these improvements through a heat low
19 mechanism.

20 **Keywords:** tropical rainfall climatology, monsoons, global coupled models, surface albedo,
21 heat low, deserts

22 1. Introduction

23

24 The monsoon systems across the Northern Hemisphere (NH) can be interpreted as the
25 seasonal swings over land of the large-scale Inter-Tropical Convergence Zone (ITCZ) cells
26 due to the intense solar heating of the northern continents during boreal summer (Schneider et
27 al. 2014). The monsoon rainfall in these complex land-atmosphere-ocean systems provides
28 fresh-water for people who live in Africa, America, South and East Asia and the fate of these
29 monsoons in a global warming environment is of great concern for about one-half of the
30 world population (IPCC 2013).

31 Yet, despite decades of intensive research to address these issues, which have important
32 socio-economic implications, almost all climate and weather prediction Coupled General
33 Circulation Models (CGCMs) still fail in capturing correctly even the basic characteristics of
34 the boreal summer monsoon systems such as their precipitation pattern and amplitude
35 (Richter et al. 2012; Roehrig et al. 2013; Sperber et al. 2013; Prodhomme et al. 2014, 2016).
36 The multi-model mean from CGCMs participating in phase 5 of the Coupled Model Inter-
37 comparison Project (Taylor et al. 2012; CMIP5) is, for example, affected by a severe dry bias
38 over South and East Asia, central America and West Africa and an opposite wet bias over the
39 adjacent oceans, reflecting a too equatorward simulated position of the ITCZ during boreal
40 summer (Fig. 1a). The CMIP models also exhibit a double ITCZ problem over the tropical
41 Pacific (Fig. 1a; Lin 2007; Reichler and Kim 2008). These tropical rainfall biases are well
42 above the rainfall standard deviation computed across the CMIP5 models in most oceanic and
43 land regions (see the contours in Fig. 1a) attesting the robustness of these errors. The only
44 exception is the land areas where orography is important, such as the foothills of the
45 Himalayas. Thus, the amplitude of the dry bias, especially in these orographic regions, is also
46 partly dependent on the horizontal resolution of the CMIP5 models (Johnson et al. 2016).

47 Furthermore, climate projections performed by the CMIP models are highly uncertain and
48 even disagree for the sign of the rainfall anomalies over the Sahel region (Roehrig et al. 2013;
49 Biasutti 2013). Over South Asia, most of the CGCMs project increasing precipitation in a
50 future warming scenario, but decreasing large-scale circulation and thermodynamic drivers of
51 the monsoon (Sooraj et al. 2015; Sabeerali et al. 2015). Thus, it has become a common belief
52 that these rainfall projections are unreliable because current CGCMs have not reached yet a
53 sufficient degree of maturity as far as the West African and Indian monsoons are concerned

54 (Roehrig et al. 2013; Sabeerali et al. 2015; Annamalai et al. 2015).

55 The Climate Forecast System version 2 (CFS; Saha et al. 2014), which is the current
56 operational climate prediction model for seasonal prediction in the US (at the National
57 Centers for Environmental Prediction, NCEP) and in India (as part of the Monsoon Mission
58 program see url: <http://www.tropmet.res.in/monsoon/>), and the SINTEX-F2 CGCM
59 (SINTEX; Masson et al. 2012), which is also a standard tool to forecast and simulate tropical
60 variability (Doi et al. 2016) share exactly the same rainfall biases (Figs. 1b and c) despite of
61 having a higher horizontal resolution than most CMIP5 models (see Section 2).
62 Consequently, these rainfall errors do not only concern climate models, but also seasonal
63 dynamical forecasting systems, thus adversely affecting the monsoon dynamical prediction
64 skill (Kim et al. 2013).

65 While increasing horizontal atmospheric resolution may help to reduce these biases
66 (Prodhomme et al. 2016), these recurrent problems of state-of-the-art CGCMs reflect also our
67 lack of understanding of the physical processes regulating the boreal summer monsoon
68 rainfall characteristics (Annamalai et al. 2015; Hourdin et al. 2015; Johnson et al. 2016). So
69 far, these rainfall biases have been attributed to regional Sea Surface Temperature (SST)
70 errors (Roehrig et al. 2013; Richter 2015; Bollasina and Ming 2013; Levine et al. 2013) and
71 deficiencies in the representation of sub-grid scale processes, especially convection and cloud
72 parameterization schemes in too coarse atmospheric models (Sabeerali et al. 2015; Dai 2006;
73 Stephens et al. 2010). In contrast, the role of land surface processes in the dry monsoon bias
74 has received less attention, despite pioneering investigations have suggested that these
75 processes have a significant influence on large-scale circulation over arid regions and the
76 monsoons (Charney et al. 1977; Sud and Smith 1985). Subsequently, many studies have
77 addressed the question of land, orography and Earth's continental configuration forcing on
78 the monsoons, but not in the perspective of reducing model biases (Dirmeyer 1998;
79 Chakraborty 2002; Liang et al. 2005a; Boos and Kuang 2010; Wu et al. 2012 among many
80 others). Recently, there are a few regional studies suggesting that improving the
81 representation of land surface processes in CGCMs or regional models may offer a way of
82 advancing their performance and skill for the NH monsoons (Alessandri et al. 2007; Richter
83 et al. 2012; Kelly and Mapes 2010; Boos and Hurley 2013; Samson et al. 2016; Ashfaq et al.
84 2016).

85 Here, we demonstrate that land surface albedo and temperature errors play a significant
86 and global role in the spurious southward ITCZ position over the monsoon regions during
87 boreal summer in current CGCMs. Our work raises the possibility that important errors in
88 land surface parameterization may explain a large part of the systematic tropical rainfall
89 errors in state-of-the-art CGCMs.

90 The article is organized as follows. In section 2, we give a brief overview of the datasets,
91 the collection of CMIP5 models and the two CGCMs used in our dedicated sensitivity
92 coupled experiments. Section 3 is devoted to an analysis of rainfall, Sea Level Pressure
93 (SLP), surface temperature, albedo and radiation biases during boreal summer in state-of-the-
94 art CGCMs suggesting that tropical rainfall errors in current CGCMs are partly associated
95 with insufficient surface thermal forcing and incorrect representation of the surface albedo
96 over the NH continents. Section 4 focuses more specifically on the role of the surface land
97 albedo and skin temperature biases on the rainfall and atmospheric circulation biases during
98 boreal summer with the help of dedicated experiments with two state-of-the-art CGCMs.
99 Conclusions and prospects for future work are given in section 5.

100

101 **2. Datasets, climate models and sensitivity coupled experiments**

102

103 Almost all our analysis and diagnostics pertain to the boreal summer season (June to
104 September, JJAS).

105

106 ***2.a Satellite-based and reanalysis datasets***

107

108 To compare model outputs with observations, we make use of three observational datasets:
109 1) monthly-accumulated precipitation from the Global Precipitation Climatology Project
110 (GPCP version 2.1; Huffman et al. 2008) over the 1979-2010 period; 2) monthly-mean
111 atmospheric variables (e.g. surface temperature, wind, SLP and sensible heat flux) derived
112 from the 0.75° ERA-Interim reanalysis, the latest global atmospheric reanalysis produced by
113 the European Centre for Medium-Range Weather Forecasts (Dee et al. 2011; data available at
114 url: <http://apps.ecmwf.int/datasets/data/interim-full-daily>), over the 1979-2014 period, and,
115 finally, 3) monthly-mean surface and Top-Of-the-Atmosphere (TOA) radiative fluxes

116 computed from the Clouds and Earth's Radiant Energy System (CERES; Energy Balance and
117 Filled (EBAF) top-of-the atmosphere and surface fluxes version 2.8; Kato et al. 2013)
118 obtained from the NASA Langley Research Center over the 2000-2014 period from url:
119 <http://ceres.larc.nasa.gov/products.php?product=EBAF-Surface>.

120 Since there are uncertainties in the observations, especially for rainfall, we have also
121 cross-validated our analyses with the Climate Prediction Center (CPC) Merged Analysis of
122 Precipitation (CMAP; Xie and Arkin 1997). Despite of the fact that CMAP produces higher
123 tropical rainfall over the ocean than GPCP due to the use of atoll data in CMAP (Yin et al.
124 2004), the results are very similar if we use CMAP as a reference in our analyses (not
125 shown), demonstrating that the CGCM rainfall biases, which we are discussing here are much
126 higher than the uncertainties in the rainfall observations. However, since GPCP is believed to
127 be much more reliable than CMAP for tropical rainfall (Yin et al. 2004), we only show the
128 results using GPGP in this study.

129 The CERES-EBAF data are commonly used for model output evaluation, since they
130 include albedo estimates for both land and ocean, and are produced by deriving the energy
131 balance from Aqua, Terra and geostationary satellites, and adjusting it to that inferred from
132 the measured warming of the oceans (Loeb et al. 2012; Kato et al. 2013). A complete
133 description of the data is available in the CERES website (url: <http://ceres.larc.nasa.gov>).

134 For our numerical experiments with updated snow-free background diffuse albedo over
135 land (described in section 2.b), we make use of the Moderate Resolution Imaging Spectro-
136 radiometer (MODIS) snow-free gap-filled white-sky (diffuse) albedo product MCD43GF-v5
137 (Schaaf et al. 2011) for three different spectral bands: total short-wave (SW, 0.3–5.0 μm),
138 visible (VIS, 0.3–0.7 μm), and near-infrared (NIR, 0.7–5.0 μm). This product is generated by
139 merging data from the Terra and Aqua platforms produced every 8 days, with 16-days
140 acquisition and available on a 0.05° global grid for land surface only. Like any algorithm to
141 derive surface broadband albedo from polar-orbit satellite observations, MODIS used three
142 steps to estimate surface albedo: atmospheric correction, Bidirectional Reflectance
143 Distribution Function (BRDF) angular modeling and narrow-to-broadband conversions.
144 Since MODIS is based on BRDF modeling specifically developed for land surface, MODIS
145 albedo datasets do not include background surface albedo for the ocean, excepted for few
146 points where ocean depth is relatively small (Schaaf et al. 2011). Moreover, it is important to
147 note that some regions are systematically masked by clouds, which makes direct albedo

148 measurements difficult, or even impossible. A temporal interpolation has been applied to fill
149 these missing values. The MODIS snow-free climatology for the three different bands is
150 computed over the 2003-2013 period. The accuracy of this product is about 2% when
151 compared to ground observations. More details about satellites, data processing and quality
152 controls of the MODIS data can be found in Schaaf et al. (2011).

153

154 ***2.b Coupled models and numerical experiments***

155

156 In order to assess precipitation, temperature and albedo biases of current CGCMs, we first
157 used the monthly mean output from CMIP5 models (Taylor et al. 2012) available at url:
158 http://cmip-pcmdi.llnl.gov/cmip5/data_portal.html. We analyze the twentieth century
159 simulations of 36 CMIP5 models (Table 1) and for all the models we use the first ensemble
160 member (“r1i1p1” from CMIP5 database) for each model. The albedo is calculated as the
161 ratio between the upward and downward shortwave radiations at the surface as obtained from
162 CMIP5 model outputs. The 20-year mean during 1980-1999 in these historical simulations
163 defines the present-day climatology for CMIP5 models.

164 For our numerical sensitivity experiments, we used two state-of-the-art CGCMs, the
165 SINTEX_F2 and CFSv2 coupled models (SINTEX and CFS hereafter). A comprehensive
166 description of SINTEX can be found in Masson et al. (2012). Its main components relevant
167 for our study are summarized as follows. The atmosphere model is ECHAM5.3 and is run at
168 T106 spectral resolution (about 1.125° by 1.125°) with 31 hybrid sigma-pressure levels
169 (Roeckner et al. 2003). The oceanic component has a horizontal resolution of ~0.5°, 31
170 unevenly spaced vertical levels and includes an ice model. Atmosphere and ocean are
171 coupled, without any flux corrections, every 2 h. The second coupled model used here is the
172 Climate Forecast System version 2 (CFS) developed by the National Centers for
173 Environmental Prediction (NCEP) and used currently for seasonal forecasting in the US and
174 India (Saha et al. 2014). Its atmospheric model, the Global Forecast System (GFS) is run at
175 T126 spectral resolution (about 0.9° by 0.9°) with 64 sigma-pressure hybrid levels. Its
176 oceanic component has a 0.25–0.5° horizontal resolution, 40 vertical levels and includes an
177 ice model. The atmosphere and ocean exchange quantities such as heat and momentum fluxes
178 every half an hour, with no flux adjustment or correction. See Saha et al. (2014) for further

179 details on the CFS model and its components.

180 Snow free albedo parameterization in CGCMs is based on the assumption that surface
181 albedo is primarily an intrinsic property of surface characteristics, depending also (for some
182 models, but not all) on the angular and spectral distributions of the incident solar radiation,
183 but that its dependence on atmospheric conditions has a relatively minor effect.

184 The land surface scheme in ECHAM5.3 (the atmospheric component of SINTEX) uses a
185 background white-sky (e.g. diffuse) SW albedo without any seasonal or diurnal cycle over
186 snow-free land surfaces (Roeckner et al. 2003). These albedos are prescribed from fixed
187 tabulated values depending only on a land cover classification. This classification contains 74
188 land use classes and for each class mean values for background surface albedo, fractional
189 vegetation cover and other vegetation properties are provided. This information is
190 subsequently aggregated to the model grid scale by averaging the vegetation parameters of all
191 land cover types, which are located in one model grid cell for the chosen resolution. Thus, the
192 albedo over snow-free land surfaces in ECHAM5.3 may be considered as a fixed boundary
193 land condition and stays constant for each grid-point at each time step of the simulation.

194 Finally, the surface albedo of a model grid box is derived as the area weighted linear
195 average of the background albedo over the fraction with snow-free land, the albedo over the
196 water fraction and the albedo over snow-covered grid area. A more comprehensive
197 description of the ECHAM5.3 albedo parameterization can be found in Roeckner et al.
198 (2003). This scheme was intended for broadband solar flux and made no differentiation
199 between direct and diffuse fluxes (beams) or spectral bands, which is a strong limitation of
200 the ECHAM5.3 model.

201 The albedo parameterization in the GFS (the atmospheric component of CFS) takes into
202 account that the albedos for direct-beam and diffuse fluxes have different characteristics,
203 especially that the direct albedo does depend on the Solar Zenith Angle (SZA) and thus do
204 vary during the day (Hou et al. 2002). Furthermore, the diffuse albedo is prescribed
205 differently for the ultraviolet and visible band (VIS, $<0.7 \mu\text{m}$) and the near-infrared band
206 (NIR, $>0.7 \mu\text{m}$) and its seasonal variations, as well as its “strong” or “weak” dependency to
207 the SZA, are also taken into account in addition to its spatial variations associated with the
208 different vegetation types (Hou et al. 2002). The direct beam albedo, which strongly depends
209 on the SZA, is then parameterized from the prescribed diffuse albedo for each spectral band
210 (e.g. VIS and NIR) using a scheme described by Hou et al. (2002). Although vegetation is not

211 explicitly represented in the GFS scheme, it can be regarded as implicitly resolved by the
212 prescribed diffuse surface albedos, which vary in space and time according to the soil and
213 vegetation types. Finally, as in ECHAM5.3, GFS separately computes at each time step
214 albedos for soil, snow, and vegetation, and then estimates the total albedo of a grid box as an
215 average of these albedos weighted by the representative area fractions.

216 Both in GFS and ECHAM5.3, the prescribed land surface snow-free diffuse albedo are
217 estimated off-line and “manually” from isolated field measurements and old (more than 30
218 years for GFS) and outdated classifications of vegetation. These aspects of the two models
219 have not been modified for a long time by the developers of GFS and ECHAM. Before the
220 era of new satellite products like MODIS (Schaaf et al. 2011), getting the correct values for
221 this kind of land surface snow-free albedo was very difficult as we will demonstrate in the
222 next section.

223 The type of albedo parameterization we have described above is typical of seasonal
224 forecasting and “simple” coupled models currently in use. This differs from Earth System
225 Models (ESMs) and many CMIP5 models in which the surface snow-free diffuse and direct
226 albedos are usually parameterized from a vegetation and soil classification (eventually
227 evolving dynamically in time) through a table (or a land model) giving the correspondences
228 between soil and vegetation categories (e.g. Plant Functional Types or biomes) and
229 background surface snow-free albedo values (Houldcroft et al. 2009). In many cases, the
230 snow-free land albedo for each biome is explicitly computed as a function of foliage density
231 and of a minimum prescribed albedo, which corresponds to the maximum of foliage density
232 for this biome. In each continental box, a fixed (or dynamical) mosaic of prescribed biomes
233 can coexist and the snow-free albedo of that box can be estimated by a surface-weighted
234 average of the albedos of the coexisting biomes (Houldcroft et al. 2009; Vamborg et al.
235 2014).

236 Finally, note that the standard output from most global climate models includes monthly
237 averaged reflected and incoming total SW radiation fluxes at surface and their ratio is defined
238 as the monthly averaged albedo. This would be consistent with the albedo computed from the
239 CERES-EBAF dataset described above and may differ from the background snow-free
240 diffuse albedo from MODIS and prescribed in the models.

241 We first run 210-years and 80-years control experiments (named SINTEX and CFS,
242 respectively) with the standard configuration of SINTEX and CFS, respectively. These

243 reference simulations are then compared with several sensitivity experiments for each
244 coupled model. Table 2 summarizes all the model simulations used in this study.

245 To examine first the role of land albedo on the monsoon dry biases, sensitivity
246 experiments were performed by setting to zero everywhere the snow-free background land
247 albedo in the two models (ZERO_SINTEX and ZERO_CFS, respectively). ZERO_SINTEX
248 and ZERO_CFS have been time integrated over a period of 60 and 30 years, respectively.

249 To evaluate the impact of the errors associated with prescribed tabulated albedo values in
250 ECHAM5.3, we have replaced these annual background albedos by a weekly climatology of
251 white-sky (e.g. diffuse) albedo for total SW broadband from the MODIS MCD43GF-v5
252 product. A seasonal cycle of the background broadband SW albedo has also been
253 incorporated since previous works have demonstrated the significance of this seasonal cycle
254 (Liang et al. 2005b; Yang et al. 2008). Similarly, the seasonally prescribed tabulated diffuse
255 albedo values for the VIS and NIR bands in GFS (four seasons are used) have been replaced
256 by corresponding estimates from MODIS MCD43GF-v5 product. In GFS, the snow-free
257 diffuse albedo values are changed daily by linear interpolation from these prescribed mean
258 seasonal climatological data and these aspects have not been modified. The sensitivity of the
259 simulated climate to these new background albedo parameterizations implemented in the
260 models is assessed with the help of two climate simulations of 110 years for
261 MODIS_SINTEX and 60 years for MODIS_CFS.

262 Finally, two simulations were performed using again a land background diffuse albedo
263 from MODIS MCD43GF-v5 product and where, in addition the land background diffuse
264 albedo has been further decreased by -0.2 over the Sahara, Arabia and Middle-East deserts
265 (domain: latitude 15°-40°N, longitude 20°W-75°E). These two simulations
266 DESERT_SINTEX and DESERT_CFS have been time integrated for a period of 60 and 30
267 years, respectively.

268 It is important to highlight that the MODIS configuration implemented in our two coupled
269 models really represents an upgrade of these CGCMs as we will demonstrate in the following
270 sections. On the other hand, the ZERO and DESERT experiments described above must be
271 considered as idealized experiments useful for illustrating, respectively, the potential
272 maximum effect and the main mechanisms associated with the changes of the background
273 snow-free albedo.

274 All the sensitivity experiments are initialized exactly as their respective control runs. For
275 SINTEX, the initial atmospheric conditions are taken as January climatologies computed
276 from ERA15 reanalysis (this is the standard initialization procedure of the ECHAM model,
277 the atmospheric component of SINTEX, as given by the developers of this model) and the
278 ocean starts from rest, initialized by a mean Levitus T–S field. For the land, the standard
279 initialization and prescribed climatology files (for parameters like soil wetness, snow depth,
280 surface roughness length, field capacity of soil, vegetation and soil types, leaf area index,
281 vegetation ratio) of the ECHAM model have also been used. For the CFS, all the experiments
282 are coupled free-runs initialized from initial conditions of 31 July 2014 taken from the CFSv2
283 Operational Analysis or Climate Data Assimilation System (CDAS) developed at NCEP (see
284 [url:https://data.noaa.gov/dataset/climate-forecast-system-version-2-cfsv2-operational-analysis](https://data.noaa.gov/dataset/climate-forecast-system-version-2-cfsv2-operational-analysis)
285). Also both models employ fixed CO₂ concentrations corresponding to present-day
286 conditions.

287 The surface temperature drift and TOA imbalance in the two models can be summarized
288 as follow. SINTEX has only a small positive TOA energy imbalance (0.17 W/m²), which is
289 fairly constant during the control simulation and, consistently, a very small positive
290 temperature drift (about 0.3-0.4°C for the surface mean global temperature for the 210 years).
291 MODIS_SINTEX exhibits a similar global temperature evolution, with a constant
292 temperature offset, during its whole integration. On the other hand, DESERT_SINTEX and
293 ZERO_SINTEX exhibit a rapid warming drift at the beginning of the integrations (about 10
294 years) and are going progressively in a small positive temperature drift after. This behavior is
295 consistent with the facts that the SINTEX model is a “well-tuned” climate model and that it
296 adjusts progressively to the increased absorbed solar radiation by the land surface all year
297 round. Note, however, that the deep ocean may take several hundred of years to reach
298 equilibrium meaning that the DESERT_SINTEX and ZERO_SINTEX experiments,
299 especially ZERO_SINTEX, are transient runs.

300 On the other hand, the CFS control run has a fairly constant TOA energy imbalance of
301 about 5.4 W/m² and is affected by a negative surface temperature drift during the first 10-20
302 years of simulation and is stabilized hereafter. These two features are well known problems
303 in the CFSv2 model (see Swapna et al. 2015; for further details) and suggest that some
304 sources of energy are not tracked correctly in CFSv2. Interestingly, the initial negative
305 temperature drift is partly or fully corrected in the MODIS_CFS, DESERT_CFS and
306 ZERO_CFS experiments, so these experiments are more stable than the control run (not

307 shown). This suggests that the large land surface albedo bias is an important contributor to
308 the cold surface temperature bias in CFSv2 (see also Rai and Saha 2017). Since CFS is
309 affected by an important TOA radiative imbalance, it cannot be considered as a climate
310 model even though CMIP simulations have also been performed with CFS (Saha et al. 2014).
311 However, our investigation does not focus only on biases of CMIP5 or climate models, but
312 also on biases in seasonal forecasting coupled models currently in use and the CFS is
313 probably one of the best examples in this category, which justifies its use here. CFS coupled
314 free-runs, as done here, have been performed in many studies and are especially useful to
315 diagnose model's errors in the US and India forecasting systems based on the CFS (Goswami
316 et al. 2014; Swapna et al. 2015; Rai and Saha 2017 among many others).

317 The differences between the sensitivity and control experiments for each model are taken
318 as the model response to the change of the background snow-free land albedo. For the
319 SINTEX experiments, all the analyses presented in the following sections exclude the first 10
320 years of the simulations to let the coupled simulations spin-up. For the CFS model, which is a
321 seasonal forecasting coupled model, data from the first 5 years of each simulation are
322 disregarded from the analyses. However, in both cases, results are robust and do not depend
323 on if more data is excluded from the start of the simulations (not shown).

324 A local statistical test is applied to the various differences fields in order to assess the
325 statistical significance of the results and to take into account the intrinsic internal variability
326 of the models. More precisely, the statistical significance of the differences was estimated
327 through the procedure in Noreen (1989), based on a permutation test with 9999 shuffles, and
328 differences significant at the 95% confidence level are indicated in the figures. More details
329 about this statistical test are given in Terray et al. (2003). The robustness of the responses is
330 also attested by the similarity of the results between the two models rather than by standard
331 statistical significance, which can be physically misleading.

332

333 **3. Rainfall, temperature, SLP and albedo biases in state-of-the-art coupled models.**

334

335 Our main investigation is based on two state-of-the-art global CGCMs (CFS and SINTEX,
336 see section 2 for details), which allow a full interplay between ocean dynamics, land
337 processes, radiation, atmospheric convection and geography of the continents. As pointed out
338 in the introduction, the boreal summer rainfall climatology of these two models is very
339 similar with those of the CMIP5 CGCMs and exhibits the same systematic errors (Figs. 1b

340 and c). These two CGCMs also exhibit systematic errors similar to CMIP5 models in
341 simulating global SSTs and SLPs during boreal summer (Fig. 2, SLP in contours). As an
342 illustration, all the models display a cold tongue bias over the equatorial Pacific (Reichler and
343 Kim 2008) and a strong overestimation of SST over the eastern tropical Pacific and Atlantic
344 oceans (Hourdin et al. 2015; Richter 2015). Numerous studies have suggested that these SST
345 errors are important for explaining the misrepresentation of the monsoons or the Pacific ITCZ
346 in current CGCMs (Roehrig et al. 2013; Prodhomme et al. 2014; Lin 2007; Reichler and Kim
347 2008; Bollasina et Ming 2013; Levine et al. 2013; Dai 2006; Wang et al. 2014; Sandeep and
348 Ajayamohan 2014), but without providing a way forward to correct these SST errors in
349 current CGCMs.

350 Interestingly, surface temperature biases over the NH continents are much larger than SST
351 biases over the adjacent oceans and exhibit some consistency across CGCMs (Fig. 2).
352 Specifically, there are large cold biases associated with positive SLP errors over the Sahara,
353 Arabia and Middle-East deserts and mid-to-high latitudes of Asia, while warm biases prevail
354 over South Asia, Sahel and Amazon Basin consistent with the deficient boreal summer
355 monsoon rainfall over these regions. In order to understand the origins of these consistent
356 temperature and SLP biases over land, we first examine the simulated surface downward
357 shortwave radiation and albedo, which control the energy budget of the land surface. CMIP5
358 and CFS models simulate excessive surface downward shortwave radiation over most of the
359 NH continents during boreal summer in agreement with previous studies (Wild et al. 2015),
360 while SINTEX exhibits reduced surface shortwave radiation in the northern high latitudes,
361 but again excessive surface shortwave radiation over land between the Equator and 50°N
362 compared to satellite estimates (Fig. 3). Obviously, the excessive downward surface
363 shortwave radiation biases over the NH continents cannot explain the cold bias found over
364 the same regions in the CGCMs during boreal summer (Fig. 2).

365 Numerous studies have found serious discrepancies between albedo observed from
366 satellite products and simulated by CGCMs, but the focus has been mainly on the snow
367 albedo feedback or the Arctic sea-ice albedo and their large spreads in CGCMs (Karlsson and
368 Svenson 2013; Thackeray et al. 2015). For boreal summer, the land albedo modeled by
369 CMIP3 models is systematically overestimated by as much as 5% despite most of the NH
370 continents are snow-free during this season (Wang et al. 2006). Errors in total surface albedo
371 for CMIP5, SINTEX and CFS models during boreal summer are presented in Figure 4.
372 Despite many CMIP5 models being full Earth-System Models (Taylor et al. 2012), current

373 CGCMs continue to exhibit systematic positive albedo biases over the NH continents (Fig. 4)
374 leading to improperly simulated land-sea temperature contrasts during boreal summer (Fig.
375 2). The positive bias is particularly strong over the NH high latitudes, the Tibetan Plateau and
376 the Middle-East. Additionally, SINTEX and CFS also show important positive albedo biases
377 over the Sahara (Fig. 4). Models have also important difficulties in simulating the strong
378 gradients of surface albedo, especially over Africa north of the Equator.

379 Snow-free albedo is determined by surface characteristics, such as vegetation and soil
380 composition, but also depends on the angular and spectral distributions of the incident solar
381 flux (Stephens et al. 2015). In CGCMs, it is either totally prescribed, as a parameter
382 dependent on land cover types, or partially simulated as an internal variable based on
383 simplified radiative transfer schemes for vegetation and bare soils (Dickinson 1983). The
384 snow-free land albedo parameterizations in SINTEX and CFS use prescribed tabulated
385 background diffuse albedo values (see section2) and Figure 5, which displays errors in snow-
386 free land background diffuse albedo for SINTEX and CFS models compared to MCD43GF-
387 v5 product from MODIS, demonstrates that these prescribed values exhibit the same
388 important positive biases as the modeled albedo during boreal summer (Fig. 4). This suggests
389 that the table giving the correspondence between albedo and vegetation types and/or the
390 classification of vegetation used to derive the albedo datasets in these models, are severely
391 biased.

392

393 Climate models are very sensitive to the specification of the surface albedo since it is
394 strongly affecting the radiation budget of the earth (Stephens et al. 2015). However, the
395 hemispheric biases in TOA net radiation budget during boreal summer are very different in
396 CFS and SINTEX despite of the similarity of the boreal summer rainfall dry biases over land
397 in these two models (see Table 3). Moreover, CFS does not follow the paradigm that tropical
398 rainfall must shift toward the relatively warmer hemisphere (Schneider et al. 2014). This
399 suggests that a TOA hemispheric energetic framework as advocated in some studies
400 (Haywood et al. 2016) is not sufficient to explain the rainfall biases in these two models.
401 Nonetheless, monsoon systems are also driven by regional moist static energy and
402 temperature contrasts between the ocean and continent (Dai et al. 2013; Nie et al. 2010) and
403 even small errors in simulated land surface albedo may contribute significantly to the dry
404 monsoon rainfall and cold temperature biases (Figs. 1 and 2). This close relationship between

405 land albedo and the intensity of the monsoon is already illustrated by several studies, which
406 used the land surface albedo as a tuning parameter to control the strength of the African and
407 Asian summer monsoons (Richter et al. 2012; Kelly and Mapes 2013). In the next sections,
408 we show through a large set of coupled model sensitivity experiments and an analysis of
409 CMIP5 models that the tropical monsoon related rainfall biases are partly related to the skin
410 temperature biases over land, especially over the NH subtropical desert regions.

411

412 **4. Numerical experiments with global coupled models**

413

414 *4.a Assessing the role of land albedo through idealized numerical experiments*

415

416 In order to illustrate the potential role of land albedo on the monsoon dry bias in current
417 CGCMs, we examine first the response of the monsoon systems to an idealized modification
418 by setting to zero everywhere the prescribed snow-free land diffuse albedo used in CFS and
419 SINTEX (see section 2 and Table 2 for details). Obviously, these experiments (ZERO_CFS
420 and ZERO_SINTEX, respectively) are designed to increase the land thermal forcing during
421 boreal summer, which is significantly deficient in the two models as in CMIP5 models (Fig.
422 2). These experiments never represent the reality, but are useful to assess whether and how
423 changes in land albedo affect tropical precipitation in state-of-the-art CGCMs.

424 The precipitation, temperature and TOA net radiation changes in these ZERO simulations
425 are entirely consistent despite of the very different physical packages included in the two
426 models (Fig. 6). Overall, the impact of a dark continent is to increase boreal summer
427 precipitation over South and East Asia, and West Africa (Figs. 6a and d). This is especially
428 true in ZERO_CFS where the ITCZ has shifted by about of 4° and is located around 10°N
429 over the South Asia and West Africa regions (Fig. 7). Precipitation also increases over the
430 eastern tropical Indian Ocean, maritime continent and at the mean position of the ITCZ in the
431 tropical Pacific, but reduces significantly over the equatorial and South Pacific in the ZERO
432 runs. Consistently, surface temperature and TOA net radiation substantially increase over the
433 NH continents, especially over the subtropical deserts and the mid-latitudes (Figs. 6b-c and e-
434 f). Thus, the ITCZ shifts in the hemisphere with greater atmospheric energy input, even if the

435 main source of atmospheric heating is outside of the tropics (Kang et al. 2008; Frierson et al.
436 2013; Schneider et al. 2014; Voigt et al. 2014). This northward shift of the rain band is
437 enough to completely reverse the land precipitation biases over West Africa and also to
438 almost remove the dry bias over South Asia found in the standard versions of the models (a
439 small negative bias of less than 1 mm/day is still there for CFS; see Fig. 8). Concerning the
440 North American monsoon system, a large rainfall increase is also seen, but it is shifted
441 westward over the Pacific Ocean in the two models instead over the land. This suggests that
442 the regional rainfall anomalies over there are not controlled by the changes of the local
443 albedo, but are a remote response to the enhanced African monsoon system to its east as
444 manifested by the strong anticyclonic circulation over the western subtropical Atlantic (see
445 Fig. 9 for details). This NH monsoon rainfall response is similar, but stronger, than in the
446 idealized experiments performed by Haywood et al. (2016) for assessing the role of excessive
447 SH energy (i.e. strong positive absorbed shortwave radiation bias) on the tropical rainfall
448 biases in current CGCMs by equilibrating the hemispheric albedos. Intriguingly, the double
449 ITCZ structure over the tropical Pacific is also significantly modified in the ZERO
450 simulations, which experience a northward shift of tropical rainfall (Figs. 6a, d and 8).

451 The ZERO simulations, where the land albedo is constant, also illustrate the important role
452 of the geometry of the continents and the orography in shaping the position of the core
453 monsoon rainfall zones (Figs. 6a and d). The surface temperature response is generally
454 consistent with the increase of absorbed solar energy by the surface, but with some important
455 exceptions. Especially, a cooling is observed over the Sahel and Indo-Gangetic areas (Figs.
456 6b and e), which we attribute to the shift and strengthening of the monsoon and the resulting
457 increase in cloud cover over these two areas (not shown).

458 The strong warming of the subtropics over land in the ZERO simulations (Figs. 6b-c and
459 e-f) affects the large-scale monsoon circulation by enhancing the tropospheric temperature
460 contrast between the continent and the adjacent oceans and also the associated vertical
461 easterly shear (Dai et al. 2013). The low-level (850-hPa) circulation response in the ZERO
462 experiments is dominated by enhanced cyclonic circulation over Africa, South and East Asia
463 (more precisely over the arid regions adjacent to the core monsoon regions during boreal
464 summer) and a related strengthening of the subtropical anticyclones to the East over the
465 Pacific Ocean and to the West over the Atlantic Ocean (Figs. 9a and c). The close connection
466 between the monsoons and the subtropical anticyclones (Rodwell and Hoskins 2001) is
467 particularly exemplified on the western flank of the North Pacific anticyclone, where the

468 moist tropical air moves poleward and feeds the East Asian monsoon. Consistent with a
469 Kelvin-wave response, the equatorial easterlies are also greatly enhanced over the western
470 and central equatorial Pacific (Gill 1980). Also, on the western flank of the monsoon cyclonic
471 center over Africa, an enhanced equatorward flow and positive SLP anomalies are found over
472 the North subtropical Atlantic. At the surface, the enhanced inter-hemispheric atmospheric
473 transport in the ZERO simulations is dominated by the northward shift of the trade winds
474 over the South Pacific, consistent with the strengthening of both the NH ITCZ and the South
475 Pacific anticyclone, and, secondary only, by a slight increase of the inter-hemispheric
476 atmospheric flux over the Atlantic Ocean (Figs. 9a and c). By contrast, a weakening of the
477 Mascarene High and inter-hemispheric flux is found in the Indian sector despite of the large
478 increase of rainfall over South Asia in the ZERO simulations.

479 The zonal asymmetry of the atmospheric response in the ZERO runs is even more evident
480 in the velocity potential fields at 200-hPa (Figs. 9b and d). The monsoon rainfall
481 improvements in the ZERO runs are actually driven by the east–west planetary differential
482 heating since at 200-hPa the divergent centers over the subtropical continents match well the
483 diabatic and sensible heating sources and are flanked by upper-level convergence centers
484 over the tropical South Pacific on one side and the western Atlantic and South America on
485 the other side. The robustness of this upper-level divergent circulation pattern is further
486 attested by the similarity of the response in the two CGCMs. These upper-level centers are
487 well coupled with the corresponding SLP centers of the same polarity in the low-level
488 circulation (Figs. 9a and c), suggesting an important role of the interactions between the
489 South Pacific subtropical anticyclone and the monsoonal heating for resolving the tropical
490 rainfall biases during boreal summer in current CGCMs.

491 Hence, the atmospheric response to the change of the surface albedo in global CGCMs is
492 very different from an uniform shift and strengthening of the Hadley circulation as found in
493 aqua-planet or simple conceptual model simulations, which focus mostly on the annual mean
494 circulation (Kang et al. 2008; Schneider et al. 2014; Voigt et al. 2014). The monsoon
495 circulation changes in the ZERO runs are dominated by an enhancement of the zonal
496 monsoon cyclone-subtropical anticyclone circulation driven by the east-west differential
497 heating, as expected from the revised planetary scale perspective on summer monsoon
498 circulation (Rodwell and Hoskins 2001; Chen 2003). Obviously, the complex land-sea
499 geography of the NH induces important zonally asymmetric surface forcings (via surface heat
500 fluxes and diabatic heating), which rectify drastically the atmospheric response in the ZERO

501 runs through stationary Rossby-wave transport and Kelvin-wave response (Shaw et al. 2015).
502 A simple regional Hadley cell argument cannot explain the strengthening of the subtropical
503 anticyclones over the tropical Pacific in the boreal summer circulation as simulated in the
504 ZERO runs (Rodwell and Hoskins 2001).

505 A caveat in these ZERO experiments is that we only replace a systematic dry bias in land
506 precipitation with a systematic bias in other variables such as TOA net radiation and surface
507 temperature (Figs. 6b-c and e-f; Tables 4 and 5) and also oceanic precipitation (Fig. 8). This
508 type of compensating errors is very common in such idealized coupled experiments
509 (Haywood et al. 2016). There is a deterioration of simulated boreal summer rainfall for many
510 tropical regions in the ZERO runs compared to the control runs (Figs. 10a and d). The Root-
511 Mean-Square Error (RMSE) and spatial pattern correlation with observed tropical rainfall
512 during boreal summer deteriorate substantially from control to ZERO experiments in the two
513 CGCMs, demonstrating that the ZERO simulations are less realistic than the control runs for
514 the whole tropics (Table 4). However, the results bring forward the unexplored hypothesis
515 that land albedo biases in the NH can be also potentially important to explain the dry
516 monsoon biases in CGCMs.

517

518 *4.b Using satellite land albedo improves the simulated tropical rainfall and atmospheric* 519 *circulation*

520

521 To demonstrate the realistic impact of revising the parameterization of snow-free albedo in
522 SINTEX and CFS coupled models, we now compare the control simulations with simulations
523 in which the prescribed snow-free land surface diffuse albedo in the two models has been
524 replaced with corresponding satellite snow-free albedo estimates (MODIS_SINTEX and
525 MODIS_CFS, respectively; see section 2 and Table 2). These changes really represent an
526 update of the models in contrast to the idealized ZERO experiments described in the previous
527 section.

528 First, using satellite snow-free diffuse albedo estimates instead of the prescribed and
529 outdated diffuse albedo in the two CGCMs darkens the NH continents, enhances TOA net
530 radiation at NH high- and subtropical-latitudes (Figs. 11a-b and e-f) and corrects parts of the
531 surface cold temperature bias found in the control runs (e.g. compare Figs. 2b-c and Fig. 12).

532 Surface temperature improvements are significant over Asia and Africa, but less over North
533 America suggesting that other important factors like the snow parameterization, the treatment
534 of the orography and the roughness length parameterization may be dominant in this region
535 (Fig. 12). Also the improvements in CFS are larger than in SINTEX, especially over the
536 Sahara and Arabian regions, probably because the corrected biases in the background snow-
537 free land albedo climatology used in CFS are much larger (see Fig. 5). Another possible
538 reason is that the CFS albedo parameterization is more complex, with much more
539 nonlinearities, since this model uses two different spectral bands and takes into account that
540 the albedos for direct-beam and diffuse fluxes have different characteristics (see Section 2 for
541 details). The darkening of the continents in the MODIS runs induces more rainfall over South
542 and East Asia and West Africa as in the ZERO runs (Figs. 13a and e), but leads also to large-
543 scale rainfall improvements for most tropical regions and in the SH (Figs. 10b and e).
544 Furthermore, MODIS_CFS better represents both the magnitude and spatial patterns of
545 summer monsoon precipitation over Africa and South Asia where major dry biases are seen
546 in CFS (Fig. 10b and Table 4). The rectification of the mean-state is particularly significant
547 over the Atlantic region where precipitation shift from the Gulf of Guinea to the continent
548 (Fig. 13a) and for the zonal mean precipitation over the African-Asian domain (Fig. 7a).
549 MODIS_SINTEX also shows improvements over South Asia, and in the tropical Atlantic, but
550 the amplitude of the corrections is more modest (Fig. 10e and Table 4) consistent with the
551 reduced albedo and temperature errors in SINTEX compared to CFS (Figs. 2b-c, 4b-c).

552 Consistent with these rainfall improvements, the monsoon low-level jet over the Arabian
553 Sea and East Asia is strengthened (Figs. 13b and f). These changes are associated with a SLP
554 decrease over Arabia, Middle-East and the Tibetan plateau, consistent with a stronger “heat”
555 low over these regions. Over West Africa, the low-level equatorial easterlies and inland
556 westerlies are significantly enhanced in MODIS_CFS compared to CFS, again in association
557 with a stronger Sahara heat low during boreal summer (Fig. 13b). Similar, but more modest,
558 changes in low-level winds are found in MODIS_SINTEX compared to SINTEX (Fig. 13f).

559 To further investigate the mechanism of the monsoon rainfall improvements, we now
560 focus on the upper troposphere and its dominant dynamical feature during boreal summer, the
561 Tropical Easterly Jet (TEJ; Wang 2006). The TEJ, located at about 200-hPa, 5°-25°N with
562 core speeds in excess of $25 \text{ m}\cdot\text{s}^{-1}$, stretches from Indochina to the tropical Atlantic. It
563 develops because of the strong temperature gradient that exists between the (cold) equator
564 and the (warm) subtropics in the upper troposphere during boreal summer associated with

565 deep moist convection over Asia and Northwest Pacific (Chen 2003). The TEJ plays a
566 paramount role in controlling the easterly vertical shear over developing weather disturbances
567 off the Atlantic coast of Africa and in South Asia (Mishra and Salvekar 1980; Nicholson et
568 al. 2007) and in driving the Asian monsoon (Jiang et al. 2004). The MODIS simulations show
569 an increase in the extension and strength of the TEJ from the subtropical Pacific to the
570 African continent compared to the control simulations (Figs. 13c and g) and better capture its
571 observed extension (not shown). Overall, the mean easterly vertical wind shear between the
572 lower and upper troposphere (e.g. the difference between zonal winds at 200- and 850-hPa) is
573 greatly amplified over all monsoon regions in the MODIS runs compared to the control runs
574 (Figs. 13b-c and f-g). All these features are consistent with the improved patterns of monsoon
575 precipitation, which exhibit a greater northward extension during boreal summer in MODIS
576 simulations. In turn, the enhanced diabatic heating associated with the Asian and African
577 monsoons induces also stronger upper-level convergence to the East over the South Pacific
578 and to its West over the Atlantic through the planetary-scale divergent circulation (Figs. 13d
579 and h; Voigt et al. 2014; Hawcroft et al. 2017). As in the ZERO simulations, this contributes
580 to strengthen the South Pacific anticyclone and reduce the eastward extension of the SPCZ
581 (Figs. 13a-b and e-f). Moreover, all these changes are ultimately related to the differential
582 surface thermal forcing (Figs. 11c and g) associated with the improvements of the surface
583 albedo in the MODIS experiments (Figs. 11a and e).

584 The changes of the NH monsoons in the MODIS runs also induce a systematic
585 strengthening of the SH subtropical anticyclones, which promotes blocking and stationary
586 patterns at SH mid- and high-latitudes (Figs. 13b-c and f-g). This has robust implications for
587 the SH, especially in the southern Pacific, where the surface temperature off the Antarctic
588 coast (e.g. between 140°-60°W) warms significantly in the two models (Figs. 11c and g) due
589 to latitudinal changes in ice limit (Figs. 11a and e). These SH changes are very beneficial for
590 reducing rainfall biases in the SH subtropics and mid-latitudes (Figs. 10b and e).
591 Surprisingly, these remote teleconnections also reduce the huge negative SLP biases found
592 over the subtropics and mid-latitudes of the SH (in the form of an expanded trough; see Figs.
593 2b and c) in the control experiments. We will again visit this surprising result in the next
594 section using CMIP5 models.

595 Interestingly, all these rainfall and atmospheric circulation improvements are not
596 associated with significant changes of the RMSE and spatial correlation statistics for TOA
597 net radiation at the global scale in the MODIS runs (Table 5). In line with recent studies

598 (Hawcroft et al. 2017; Kay et al. 2016), this suggests that a global or hemispheric energetic
599 framework is not necessarily the best method to reduce the tropical rainfall biases in CGCMs.

600

601 *4.c Seminal role of the heat lows over the subtropical deserts*

602

603 Finally, the higher surface temperature, lower SLPs and stronger cyclonic circulation over
604 the Sahara, Arabia and Middle-East arid regions in both the ZERO and MODIS simulations
605 suggest additionally a more regional perspective related to a “heat low” mechanism to
606 explain the improvements of the monsoons in these experiments (Cook and Vizy 2016;
607 Lavaysse 2015; Lavaysse et al. 2016; Samson et al. 2016; Ashfaq et al. 2016). Due to the
608 strong radiative cooling over arid regions, the role of these deserts is to decrease NH energy
609 content and shift the ITCZ and the monsoon southward (Frierson et al. 2013). However, in
610 the same energetic framework, the significant decrease of the surface albedo and associated
611 increase of the TOA net radiation over these arid regions in our dedicated experiments (Figs.
612 11a-b and e-f) imply a northward shift of the mean precipitation (Figs. 13a and e). This shift
613 is especially evident over the core monsoon zones in the ZERO and MODIS runs (Fig. 7).
614 This seems ultimately related to improvements in the simulated surface temperature gradients
615 between the monsoon zones over land, the neighboring arid regions (such as the Sahara and
616 Middle-East deserts) and the ocean to the South (Fig. 12) and to a stronger sensible heat flux
617 (Figs. 11d and h). Errors in prescribed snow-free diffuse albedo over the deserts (Fig. 5) may
618 cause important biases in the computation of ground temperature (Fig. 12) and surface fluxes
619 (Figs. 11d and h) because surface albedo regulates the shortwave radiation absorbed by the
620 surface. These temperature and surface fluxes errors may in turn lead to erroneous SLP and
621 circulation patterns (Figs. 13b-d and f-h), responsible for the dry biases in monsoon regions
622 (Samson et al. 2016), apart from SST errors and incorrect global TOA net radiation
623 imbalance in current CGCMs (Roehrig et al. 2013; Sandeep and Ajayamohan 2014;
624 Haywood et al. 2016). This is in full agreement with the key-role attributed to the Sahara heat
625 low for explaining the interannual and decadal variability of rainfall over West Africa,
626 including the severe long-term Sahel drought during the 1970s and 1980s and its partial
627 recovery during the recent decades (Cook and Vizy 2015; Lavaysse 2015; Lavaysse et al.
628 2016).

629 To further support the hypothesis that the NH subtropical deserts are an important factor in
630 the rectification of the dry monsoon bias in CGCMs, we run two simulations similar to the
631 MODIS runs, but with an additional artificial decrease of 0.2 of the surface diffuse albedo
632 over the Sahara, Arabia and Middle-East deserts (referred as DESERT_CFS and
633 DESERT_SINTEX; see Table 2). In both ZERO and MODIS experiments, the background
634 snow-free surface albedo is changed everywhere, in an idealized way in the ZERO
635 experiments and realistically in MODIS experiments. In both of them, the observed monsoon
636 changes seem to be linked to skin temperature and SLP changes over the hot subtropical
637 desert extending from West Africa to Pakistan and northwest India. However, an exact
638 quantification is difficult since the background snow-free albedo has been changed elsewhere
639 compared to the control runs. On the other hand, in the DESERT experiments, the only
640 modification compared to the MODIS runs is a change in the background snow-free surface
641 albedo over the NH subtropical desert. So accordingly, the DESERT experiments by
642 construction are designed to provide a more precise quantification of the relationship between
643 the strength of the monsoon systems, essentially the African and South Asian monsoon
644 systems, and climate conditions over the neighboring subtropical deserts.

645 Due to this artificial albedo decrease, these arid regions absorb more shortwave radiation
646 and, as expected, the skin temperature, upward long-wave and sensible heat fluxes are
647 substantially enhanced compared to the MODIS simulations (Figs. 14a-b and e-f). The
648 increased sensible heat flux and associated heating of the lower atmosphere are sufficient to
649 decrease furthermore the surface pressure and enhance the cyclonic vorticity over these
650 regions compared to the MODIS simulations (Figs. 14d and h). In both models, the region of
651 warm temperatures is more zonally coherent and manifests itself as a zonally elongated heat
652 trough extending from the Sahara to the Middle-East in the simulated SLP fields (Figs. 14d
653 and h). The response of the NH monsoons to the enhanced large-scale north-south SLP
654 gradient that occurs across Africa and Asia, associated with this planetary-scale heat low, is
655 illustrated in the large-scale circulation and precipitation fields simulated in the DESERT
656 runs (Figs. 14c-d and g-h). In DESERT runs, the ITCZ shifts northward compared to MODIS
657 experiments (Fig. 7), the dry bias over West Africa is again reversed into a wet bias, as in the
658 ZERO simulations, and the rainfall over South Asia is only slightly underestimated (Fig. 15).
659 Furthermore, a significant duality between the diabatic heating associated with the African-
660 Asian monsoon and the strength of the subtropical anticyclones over the Pacific and Atlantic
661 oceans is also found, as in the ZERO experiments (Figs. 14d and h). As a direct consequence,

662 the North American monsoon is, however, decreased. In these areas, a large increase of
663 rainfall is seen, but it is shifted westward over the Pacific Ocean in the two models (Figs. 14c
664 and g). The SLP and 850 hPa wind responses in the DESERT experiments confirm that the
665 drying of the North American monsoon and this westward shift of the rain band are both
666 associated with the strengthening of the North Atlantic subtropical anticyclone, which is
667 remotely forced by diabatic heating associated with the African-Asian monsoon (Figs. 14d
668 and h; Rodwell and Hoskins 2001; Rodwell and Hoskins 1996). Finally, the similarity in
669 large-scale circulation and rainfall responses in the two models (Figs. 14c-d and g-h) and the
670 large-scale rainfall improvements in the DESERT runs (Figs. 10c and f) demonstrate the
671 robustness of the role of the NH deserts on the boreal summer climate.

672 A large majority of CMIP5 models also exhibit a severe cold bias over the NH subtropical
673 deserts, as CFS and SINTEX (Fig. 16a). A substantial co-variability also exists between this
674 NH subtropical desert temperature and atmospheric variability in CMIP5 models as revealed
675 by composite differences for precipitation, SLP and 850-hPa wind between the six warmest
676 and six coldest CMIP5 models (Figs. 16b and c) and regression between tropical rainfall and
677 NH deserts surface temperature across 36 CMIP5 models (Fig. 17). The selected six coldest
678 and warmest CMIP5 models used in this composite analysis are, respectively, the six CMIP5
679 models with the highest (lowest) boreal summer land surface temperature in the domain 15°-
680 40°N and 20°W-75°E, which was used in our DESERT numerical experiments. They
681 correspond to the CMIP5 models, respectively, on the extreme left and right of the plot
682 displayed in Fig. 16a. The composite and regression results show similar rainfall and
683 atmospheric circulation responses over the West African and South Asian monsoon regions
684 as observed improvements in DESERT, ZERO and MODIS experiments with respect to their
685 control experiments (see Figs. 9, 13 and 14). They also show a consistent relationship
686 between the surface temperature over the NH subtropical deserts and the SLP variability over
687 the subtropics and mid-latitudes of the SH during boreal summer (Fig. 16c), as our numerical
688 experiments, suggesting again that the large negative SLP biases found over the SH
689 subtropics and mid-latitudes in CMIP5 models (Fig. 2a) may have remote origins in the NH.

690 However, the CMIP5 results do not show a westward shift of the North American
691 monsoon as in the ZERO and DESERT experiments (Figs. 14c and d). Over this region, the
692 CMIP5 rainfall pattern is more similar to the North American monsoon rainfall response in
693 the MODIS experiments, which seems to be more realistic (Figs. 13a and e). Furthermore, the
694 rainfall regression pattern from CMIP5 models shows also a reduction of the double ITCZ

695 over the tropical Pacific compared to our ZERO and DESERT experiments, with a decrease
696 of the rainfall biases north of the equator (Fig. 17), while our experiments show in most cases
697 a more intense ITCZ and a stronger wet bias in the North tropical Pacific (Figs. 6a and d, 14c
698 and g).

699 Despite of these differences, these results demonstrate that a change of surface albedo and
700 skin temperature over the NH subtropical deserts may lead on its own to an important
701 rectification of the ITCZ position in monsoon regions, significant atmospheric improvements
702 over the SH (in subtropics and mid-latitudes of the SH) and a modest reduction of the Pacific
703 double ITCZ during boreal summer in current CGCMs. Finally, the similarity in large-scale
704 circulation and rainfall response in our two models demonstrates the robustness of the role of
705 the NH deserts on the boreal summer climate.

706

707 **5. Conclusion and discussion**

708

709 In a very broad sense, our modeling efforts demonstrate that the monsoon dry biases over
710 the Afro-Asian region in current CGCMs are, partly, related to improper simulation of the
711 large-scale pressure gradient between the hot NH subtropical deserts and the relatively cooler
712 oceans to the South. Our results further highlight that erroneous meridional and zonal surface
713 temperature gradients over the monsoon regions in current CGCMs, while partly forced by
714 atmospheric and convection errors, are also able to drive atmospheric and rainfall biases,
715 especially away from the Equator, by geostrophic adjustments. While previous studies have
716 mostly focused on the role of SST biases (Roehrig et al. 2013; Prodhomme et al. 2014;
717 Reichler and Kim 2008; Bollasina et Ming 2013; Levine et al. 2013), here we have tested the
718 land albedo contribution to these erroneous temperature gradients and showed the associated
719 impact on the monsoon rainfall and circulation biases, a topic rarely discussed thoroughly in
720 the literature. This extends and is consistent with recent studies focusing more specifically on
721 the Indian monsoon using a tropical channel coupled model (Samson et al. 2016) or an
722 atmospheric model (Ashfaq et al. 2016). The variability of the heat lows over the NH
723 subtropical arid regions is demonstrated to modulate significantly the thermal and SLP
724 contrasts between ocean and land in our two coupled models. In most CMIP5 models, this
725 thermal contrast between the NH deserts and the oceans is considerably reduced due to weak
726 surface thermal forcing over land (Figs. 2a and 16a), which results in higher-than observed
727 surface pressures (i.e., the lows are not as deep as observed; Fig. 16c). CMIP5 models also

728 assert that the stronger the surface thermal forcing over the deserts is, the weaker are the dry
729 bias over the NH monsoon regions and the Pacific double ITCZ problem during boreal
730 summer (Figs. 16b and 17). Furthermore, the darkening of the NH arid regions in our
731 experiments highlights the significant duality between the NH monsoons and the subtropical
732 anticyclones over the Pacific and Atlantic oceans and is demonstrated to play a significant
733 role in correcting SH rainfall and SLP biases in current coupled models. Indeed, in all our
734 experiments, the Sahara, Arabia and Middle-East regions form a planetary-scale thermal low,
735 which exhibits a clear connection to the summertime Asian and African monsoon circulations
736 and the strength of the South Pacific anticyclone. Preliminary analysis shows that similar
737 large-scale improvements can be expected for the SH monsoon systems and the double ITCZ
738 problem during boreal winter (not shown).

739 This suggests that the contribution of the land and subtropical deserts to the thermal
740 forcing of the tropical climate is significantly underestimated in current CGCMs. Part of this
741 bias results from incorrect albedo parameterization, but this by no means precludes the
742 importance of other sources of errors concerning the land emissivity or roughness length,
743 which regulate the skin temperature over the deserts through the balance between the upward
744 long-wave and sensible heat fluxes (Deardorff 1978) or the soil characteristics and humidity,
745 which modulate the temperature gradient between the monsoon zones and the adjacent
746 deserts (Kumar et al. 2014).

747 Unfortunately, the energy budget over these arid regions is still afflicted with considerable
748 uncertainties, especially the poorly known sensible heat fluxes, which are often obtained as
749 residual terms from the best estimates for downward solar and thermal radiation (Wild et al.
750 2015). Due to their key importance for monsoon climates and tropical rainfall biases in
751 CGCMs, the energy budget and sensible heat flux over land must deserve more attention.
752 Understanding land processes, as well as their coupling to the large-scale circulation, and
753 improving their parameterization in current CGCMs must be considered as one of the current
754 grand challenges in climate science at the same level than the cloud-radiative feedbacks and
755 the convection (Bony et al. 2015).

756 **Acknowledgments**

757 The authors gratefully acknowledge the financial support given by the Earth System Science
758 Organization, Ministry of Earth Sciences, Government of India, to conduct this research
759 under the National Monsoon Mission (Grant #MM/SERP/CNRS/2013/INT-10/002,

760 Contribution #MM/PASCAL/RP/08). We sincerely thank Prof. Ravi Nanjundiah, Director,
761 Indian Institute of Tropical Meteorology (IITM, India) and Dr. R Krishnan, executive
762 Director, Centre for Climate Change Research (at IITM, India) for all the support during this
763 research study. We acknowledge the World Climate Research Programme's Working Group
764 on Coupled Modeling, which is responsible for CMIP, and we thank the climate modeling
765 groups (listed in the Supplementary Materials) for producing and making available their
766 model output. For CMIP, the US Department of Energy's Program for Climate Model
767 Diagnosis and Inter-comparison provides coordinating support and led development of
768 software infrastructure in partnership with the Global Organization for Earth System Science
769 Portals. Computer resources from Indian Institute of Tropical Meteorology (India) and
770 GENCI-IDRIS (France, Grants 2015, 2016, 2017 – 016895) are also acknowledged.

771

772

773 **References**

- 774 Alessandri A, Gualdi S, Polcher J, Navarra A (2007) Effects of land surface-vegetation on the
775 boreal summer surface climate of a GCM. *J. Clim.* **20**:255-278.
- 776 Annamalai H *et al.* (2015) Persistence of Systematic errors in the Asian-Australian monsoon
777 Precipitation in climate models: a way forward. *Clivar Exchanges* **66**:19-22.
- 778 Ashfaq M, Rastogi D, Mei R, Touma D, Leung RL (2016) Sources of errors in the simulation
779 of south Asian summer monsoon in CMIP5 GCMs. *Clim. Dyn.* online, doi
780 10.1007/s00382-016-3337-7
- 781 Biasutti M (2013) Forced Sahel rainfall trends in the CMIP5 archive. *J. Geophys. Res.*
782 **118**:1613–1623.
- 783 Bollasina MA, Ming Y (2013) The general circulation model precipitation bias over the
784 southwestern equatorial Indian Ocean and its implications for simulating the South
785 Asian monsoon. *Clim. Dyn.* **40**:823–838.
- 786 Bony S *et al.* (2015) Clouds, circulation and climate sensitivity. *Nat. Geosci.* **8**:261–268.
- 787 Boos WR and Kuang Z (2010) Dominant control of the South Asian monsoon by orographic
788 insulation versus plateau heating. *Nature* **463**:218–222.
- 789 Boos WR and Hurley JV (2013) Thermodynamic Bias in the Multimodel Mean Boreal
790 Summer Monsoon. *J. Climate* **26**:2279–2287.
- 791 Chakraborty A (2002) Role of Asian and African orography in Indian summer monsoon.
792 *Geophys. Res. Lett.* **29**:1989.
- 793 Charney J, Quirk WJ, Chow S, Kornfield J (1977) A Comparative Study of the Effects of
794 Albedo Change on Drought in Semi–Arid Regions. *J. Atmos. Sci.* **34**:1366–1385.
- 795 Chen T-C (2003) Maintenance of Summer Monsoon Circulations: A Planetary-Scale
796 Perspective. *J. Climate* **16**:2022-2037.
- 797 Cook KH, Vizy EK (2015) Detection and analysis of an amplified warming of the Sahara
798 desert. *J. Climate* **28**:6560–6580.
- 799 Dai A (2006) Precipitation characteristics in eighteen coupled climate models. *J. Climate*
800 **19**:4605–4630.
- 801 Dai A *et al.* (2013) The relative roles of upper and lower tropospheric thermal contrasts and
802 tropical influences in driving Asian summer monsoons. *J. Geophys. Res.* **118**:7024–
803 7045.
- 804 Deardorff JW (1978) Efficient prediction of ground surface temperature and moisture with
805 inclusion of a layer of vegetation. *J. Geophys. Res.* **83**:1889–1903. Dickinson RE (1983)

- 806 Land Surface Processes and Climate Surface Albedos and Energy-Balance. *Adv.*
807 *Geophys.* **25**:305-353.
- 808 Dee DP *et al.* (2011) The ERA-Interim reanalysis: Configuration and performance of the data
809 assimilation system. *Q. J. Roy. Meteorol. Soc.* **137**:553–597.
- 810 Dirmeyer PA (1998) Land-sea geometry and its effect on monsoon circulations. *J. Geophys.*
811 *Res.* **103**(D10):11,555-11,572.
- 812 Doi T, Behera SK, Yamagata T (2016) Improved seasonal prediction using the SINTEX-F2
813 coupled model. Extended ENSO predictions using a fully coupled ocean–atmosphere
814 model. *JAMES, online*.
- 815 Frierson DM *et al.* (2013) Contribution of ocean overturning circulation to tropical rainfall
816 peak in the Northern Hemisphere. *Nat. Geosci.* **6**:940–944.
- 817 Gill AE (1980) Some simple solutions for heat-induced tropical circulation. *Q. J. Roy.*
818 *Meteorol. Soc.* **106**:447–462.
- 819 Goswami BB, M Deshpande, P Mukhopadhyay, SK Saha, SA Rao, R Murthugudde, BN
820 Goswami (2014) Simulation of monsoon intraseasonal variability in NCEP CFSv2 and
821 its role on systematic bias. *Clim. Dyn.* **43**:2725–2745
- 822 Hawcroft M, Haywood J, Collins M, Jones A, Jones AC, Stephens G. (2017) Southern
823 albedo, interhemispheric energy transports and the ITCZ: global impacts of biases in a
824 coupled model. *Clim. Dyn.* **48**:2279–2295.
- 825 Haywood JM *et al.* (2016) The impact of equilibrating hemispheric albedos on tropical
826 performance in the HadGEM2-ES coupled climate model, *Geophys. Res. Lett.* **43**:395–
827 403.
- 828 Hou Y-T, Moorthi S, Campana KA (2002) Parameterization of solar radiation transfer in the
829 NCEP models. NCEP Office Note 441. Hourdin F, Gainusa-Bogdan A, Braconnot P,
830 Dufresne J-L, Traore A-K, Rio C (2015) Air moisture control on ocean surface
831 temperature, hidden key to the warm bias enigma. *Geophys. Res. Lett.* **42**:10,885–
832 10,893.
- 833 Houldcroft CJ, Grey WMF, Barnsley M, Taylor CM, Los SO, North PRJ (2009) New
834 vegetation albedo parameters and global fields of soil background albedo derived from
835 MODIS for use in a climate model. *J. of Hydrometeorology*, **10**:183–198
- 836 Huffman GJ, Adler RF, Bolvin DT, Gu G (2009) Improving the global precipitation record:
837 GPCP Version 2.1. *Geophys. Res. Lett.* **36**:L17808.
- 838 IPCC Fifth Assessment Report of the Intergovernmental Panel on Climate Change (2013)
839 www.ipcc.ch/ipccreports/ar4-wg1.htm.
- 840 Jiang XN, Li T, Wang B (2004) Structures and mechanisms of the northward propagating
841 boreal summer intraseasonal oscillation. *J. Climate* **17**:1022–1039.

- 842 Johnson SJ, Levine RC, Turner AG et al. (2016) The resolution sensitivity of the South Asian
843 monsoon and Indo-Pacific in a global $\sim 0.35^\circ$ AGCM. *Clim. Dyn.* **46**:807-831.
844 doi:10.1007/s00382-015-2614-1
- 845 Kang SM, Held IM, Frierson DMW, Zhao M (2008) The response of the ITCZ to
846 extratropical thermal forcing: Idealized slab-ocean experiments with a GCM. *J. Climate*
847 **21**:3521–3532.
- 848 Karlsson J, Svenson G (2013) Consequences of poor representation of Arctic sea-ice albedo
849 and cloud-radiation interactions in the CMIP5 model ensemble. *Geophys. Res. Lett.*
850 **40**:4374–4379.
- 851 Kato S *et al.* (2013) Surface Irradiances Consistent with CERES-Derived Top-of-Atmosphere
852 Shortwave and Longwave Irradiances. *J. Climate* **26**:2719–2740.
- 853 Kay JE, Wall C, Yettella V, Medeiros B, Hannay C, Caldwell P, Bitz C. (2016) Global
854 climate impacts of fixing the Southern Ocean shortwave radiation bias in the
855 Community Earth System Model. *J. Clim.* **29**:4617-4636, doi:10.1175/JCLI-D-15-
856 0358.1
- 857 Kelly P, Mapes B (2010) Land Surface Heating and the North American Monsoon
858 Anticyclone: Model Evaluation from Diurnal to Seasonal. *J. Climate* **23**:4096–4106.
- 859 Kelly P, Mapes B (2013) Asian monsoon forcing of subtropical easterlies in the Community
860 Atmosphere Model: Summer climate implications for the western Atlantic. *J. Climate*
861 **26**:2741–2755.
- 862 Kim HM, Webster PJ, Curry JA, Toma VE (2013) Asian summer monsoon prediction in
863 ECMWF system 4 and NCEP CFSv2 retrospective seasonal forecasts. *Clim. Dyn.*
864 **39**:2975–2991.
- 865 Kumar P, Podzun R, Hagemann S, Jacob D (2014) Impact of modified soil thermal
866 characteristic on the simulated monsoon climate over south Asia. *J. Earth Syst. Sci.*
867 **123**:151–160.
- 868 Lavaysse C (2015) Warming trends: Saharan desert warming. *Nat. Clim. Change* **5**:807–808.
- 869 Lavaysse C, Flamant C, Evan A, Janicot S, Gaetani, M (2016) Recent climatological trend of
870 the Saharan heat low and its impact on the West African climate. *Clim. Dyn.* **47**: 3479–
871 3498.
- 872 Levine RC, Turner AG, Marathayil D, Martin GM (2013) The role of northern Arabian Sea
873 surface temperature biases in CMIP5 model simulations and future predictions of Indian
874 summer monsoon rainfall. *Clim. Dyn.* **41**:155-172.
- 875 Liang X, Liu Y, Wu G (2005a) The role of land-sea distribution in the formation of the Asian
876 summer monsoon. *Geophys. Res. Lett.* **32**:L03708.

- 877 Liang X-Z et al. (2005b), Development of land surface albedo parameterization based on
878 Moderate Resolution Imaging Spectroradiometer (MODIS) data. *J. Geophys. Res.*
879 110:D11107, doi:10.1029/2004JD005579
- 880 Lin JL (2007) The double-ITCZ problem in IPCC AR4 coupled GCMs: Ocean-atmosphere
881 feedback analysis. *J. Climate* **20**:4497–4525.
- 882 Loeb NG *et al.* (2012) Advances in understanding top-of-atmosphere radiation variability
883 from satellite observations. *Surv. Geophys.* **33**, 359–385.
- 884 Masson S, Terray P, Madec G, Luo J–J, Yamagata T, Takahashi K (2012) Impact of intra-
885 daily SST variability on ENSO characteristics in a coupled model. *Clim. Dyn.* **39**:681-
886 707.
- 887 Mishra SK, Salvekar PS (1980) Role of barotropic instability in the development of monsoon
888 disturbances. *J. Atmos. Sci.* **37**:383–394.
- 889 Nicholson SE, Barcilon AI, Challa M, Baum M (2007) Wave Activity on the Tropical
890 Easterly Jet. *J. Atmos. Sci.* **64**:2756-2763.
- 891 Nie J, Boos WR, Kuang Z (2010) Observational evaluation of a convective quasi-equilibrium
892 view of monsoons. *J. Climate* **23**:4416–4428.
- 893 Noreen EW (1989) Computer-intensive methods for testing hypotheses: an introduction.
894 Wiley, New York
- 895 Prodhomme C *et al.* (2014) Impacts of Indian Ocean SST biases on the Indian Monsoon: as
896 simulated in a global coupled model. *Clim. Dyn.* **42**:271–290.
- 897 Prodhomme C *et al.* (2016) Benefits of increasing the model resolution for the seasonal
898 forecast quality in EC-Earth. *J. Climate* online.
- 899 Rai A, Saha SK (2017) Evaluation of energy fluxes in the NCEP climate forecast system
900 version 2.0 (CFSv2). *Clim. Dyn.* online, doi:[10.1007/s00382-017-3587-z](https://doi.org/10.1007/s00382-017-3587-z)
- 901 Reichler T, Kim J (2008) How well do coupled models simulate today’s climate? *Bull. Amer.*
902 *Meteorol. Soc.* **89**:303–311.
- 903 Richter I, Xie S-P, Wittenberg AT, Masumoto Y (2012) Tropical Atlantic biases and their
904 relation to surface wind stress and terrestrial precipitation. *Clim. Dyn.* **38**:985–1001.
- 905 Richter I (2015) Climate model biases in the eastern tropical oceans: Causes, impacts and
906 ways forward. *Clim. Change* **6**:345–358.
- 907 Rodwell MJ, Hoskins BJ (1996) Monsoons and the dynamics of deserts. *Q. J. Roy. Meteorol.*
908 *Soc.* **122**:1385–1404.
- 909 Rodwell MJ, Hoskins BJ (2001) Subtropical Anticyclones and Summer Monsoons. *J.*
910 *Climate* **14**:3192-3211.

- 911 Roeckner E *et al.* (2003) The atmospheric general circulation model ECHAM5: Part 1: model
912 description. Max-Planck-Institut für Meteorologie, Hamburg, MPI-Report 349.
- 913 Roehrig R, Bouniol D, Guichard F, Hourdin F, Redelsperger JL (2013) The Present and
914 Future of the West African Monsoon: A Process-Oriented Assessment of CMIP5
915 simulations along the AMMA Transect. *J. Climate* **26**:6471- 6505.
- 916 Sabeerali CT, Rao SA, Dhakate AR, Salunke K, Goswami BN (2015) Why ensemble mean
917 projection of south Asian monsoon rainfall by CMIP5 models is not reliable? *Clim. Dyn.*
918 **45**:161–174.
- 919 Saha S *et al.* (2014) The NCEP climate forecast system version 2. *J. Climate* **27**:2185–2208.
- 920 Samson G, Masson S, Durand F, Terray P, Berthet S, Jullien S (2016) Role of land surface
921 albedo and horizontal resolution on the Indian Summer Monsoon biases in a coupled
922 ocean-atmosphere tropical-channel model. *Clim. Dyn.* online.
- 923 Sandeep S, Ajayamohan RS (2014) Origin of the cold bias over the Arabian Sea in climate
924 models. *Scientific Reports*, **4**:6043.
- 925 Schaaf CB, Liu J, Gao F, Strahler AH (2011) Land Remote Sensing and Global
926 Environmental Change. *L. Remote Sens. Glob. Environ. Chang.* **11**:549–561.
- 927 Schneider T, Bischoff T, Haug GH (2014) Migration and dynamics of the inter-tropical
928 convergence zone. *Nature* **513**:45–53.
- 929 Shaw TA, Voigt A, Kang SM, Seo J (2015) Response of the intertropical convergence zone
930 to zonally asymmetric subtropical surface forcings. *Geophys. Res. Lett.* **42**:9961–9969.
- 931 Sooraj KP, Terray P, Mujumdar M (2015) Global warming and the weakening of the Asian
932 summer monsoon circulation: assessments from the CMIP5 models. *Clim. Dyn.* **45**:233–
933 252.
- 934 Sperber KR *et al.* (2013) The Asian summer monsoon: an inter-comparison of CMIP5 vs.
935 CMIP3 simulations of the late 20th century. *Clim. Dyn.* **41**:2711–2744.
- 936 Stephens GL *et al.* (2010) Dreary state of precipitation in global models. *J. Geophys. Res.*
937 **115**:D24211.
- 938 Stephens GL, O’Brien D, Webster PJ, Pilewski P, Kato S, Li J-I (2015) The Albedo of Earth.
939 *Rev. Geophys.* **53**:141–163.
- 940 Sud YC, Smith WE (1985) Influence of local land surface processes on the Indian Monsoon:
941 A numerical study. *J. Climate and Appl. Meteor.* **24**:1015-1036.
- 942 Swapna *et al.* (2015) The IITM earth system model. *Bull. Amer. Meteor. Soc.* **96**:1351-1367
943 doi:10.1175/BAMS-D-13-00276.1
- 944 Taylor KE, Stouffer RJ, Meehl GA (2012) An overview of CMIP5 and the experiment
945 design. *Bull. Amer. Meteorol. Soc.* **93**:485–498.

- 946 Terray P, Delecluse P, Labattu S, Terray L (2003) Sea Surface Temperature Associations
947 with the Late Indian Summer Monsoon. *Clim. Dyn.* **21**:593–618
- 948 Thackeray CW, Fletcher CG, Derksen C (2015) Quantifying the skill of CMIP5 models in
949 simulating seasonal albedo and snow cover evolution, *J. Geophys. Res.* **120**:5831–5849.
- 950 Vamborg FSE, Brovkin V, Claussen M (2014) Background albedo dynamics improve
951 simulated precipitation variability in the Sahel region. *Earth Syst. Dynam.* **5**:89-101
- 952 Voigt A, Stevens B, Bader J, Mauritsen, T (2014) Compensation of hemispheric albedo
953 asymmetries by shifts of the ITCZ and tropical clouds, *J. Climate* **27**:1029–1045.
- 954 Wang B (2006) *The Asian monsoon*. Springer-Verlag 870 pp.
- 955 Wang C, Zhang L, Lee SK, Wu L, Mechoso CR (2014) A global perspective on CMIP5
956 climate model biases. *Nat. Clim. Change.* **4**:201–205.
- 957 Wang S, Trishchenko AP, Khlopenkov KV, Davidson A (2006) Comparison of International
958 Panel on Climate Change Fourth Assessment Report climate model simulations of
959 surface albedo with satellite products over northern latitudes, *J. Geophys. Res.*
960 **111**:D21108.
- 961 Wild M *et al.* (2015) The energy balance over land and oceans: an assessment based on direct
962 observations and CMIP5 climate models. *Clim. Dyn.* **44**:3393–3429.
- 963 Wu G *et al.* (2012) Thermal Controls on the Asian Summer Monsoon. *Scientific Rep.* **2**:1–7.
- 964 Xie, P, Arkin, PA (1997) Global precipitation: A 17-year monthly analysis based on gauge
965 observations, satellite estimates, and numerical model outputs. *Bull. Amer. Meteor. Soc.*
966 **78**:2539–2558
- 967 Yang F, Mitchell K, Hou Y-T, Dai Y, Zeng X, Wang Z, Liang X-Z (2008) Dependence of
968 Land Surface Albedo on Solar Zenith Angle: Observations and Model Parameterization.
969 *J. Appl. Meteor. Clim.* **47**:2963-2982.
- 970 Yin et al. (2004) Comparison of the GPCP and CMAP Merged Gauge–Satellite Monthly
971 Precipitation Products for the Period 1979–2001. *J. of Hydrometeorology* **5**:1207-1222

972 **Figure Captions**

973 **Figure 1:** Rainfall biases (mm/day, shading) during boreal summer (e.g. from June to
974 September) in **(a)** ensemble-mean from 36 CMIP5 CGCMs (see **Table 1**), **(b)** SINTEX-F2
975 coupled model (Masson et al. 2012) and **(c)** Climate Forecast System version2 (CFS) coupled
976 model (Saha et al. 2014) against monthly-accumulated precipitation from the Global
977 Precipitation Climatology Project (Huffman et al. 2009) over the 1979-2010 period. The
978 boreal summer rainfall standard deviation in the 36 CMIP5 CGCMs is also shown as
979 contours (interval every 0.5 mm/day) in panel **(a)**.

980
981 **Figure 2:** Skin temperature ($^{\circ}\text{C}$, shading) and SLP (hPa, contours every 1-hPa) biases during
982 boreal summer (e.g. from June to September) in **(a)** ensemble-mean from 36 CMIP5 CGCMs
983 (see **Table 1**), **(b)** SINTEX coupled model and **(c)** CFS coupled model against ERA-Interim
984 reanalysis estimates (Dee et al. 2011) over the 1979-2014 period.

985
986 **Figure 3:** Surface downward shortwave radiation biases (W/m^2) during boreal summer (e.g.
987 from June to September) in **(a)** ensemble-mean from 36 CMIP5 CGCMs (see **Table 1**), **(b)**
988 SINTEX and **(c)** CFS coupled models against estimates from the CERES-EBAF version 2.8
989 dataset (Kato et al. 2013). The CERES_EBAF boreal summer climatology is estimated from
990 the period 2000-2014.

991
992 **Figure 4:** Surface albedo biases (%) during boreal summer (e.g. from June to September) in
993 **(a)** ensemble-mean from 36 CMIP5 CGCMs (see **Table 1**), **(b)** SINTEX coupled model and
994 **(c)** CFS coupled model against radiative fluxes estimates computed from the Clouds and
995 Earth's Radiant Energy System (CERES) system (Kato et al. 2013) over the 2000-2014
996 period.

997
998 **Figure 5:** Background snow-free albedo biases (%) over land during boreal summer (e.g.
999 from June to September) for **(a)** diffuse broadband Short-Wave (SW, $0.3\text{--}5.0\ \mu\text{m}$) albedo in
1000 SINTEX CGCM, **(b)** diffuse Near-Infra-Red (NIR, $>0.7\ \mu\text{m}$) albedo in CFS CGCM and **(c)**
1001 diffuse Visible (VIS, $<0.7\ \mu\text{m}$) albedo in CFS CGCM against corresponding estimates from
1002 the Moderate Resolution Imaging Spectro-radiometer (MODIS) snow-free gap-filled white-
1003 sky (diffuse) albedo product MCD43GF-v5 (Schaaf et al. 2011). The MODIS climatologies
1004 are estimated from the 2003-2013 period. See section 2 for further details.

1005

1006 **Figure 6:** Boreal summer (e.g. from June to September) differences between the ZERO and
1007 control experiments (see **Table 2**) for CFS (**a,b,c**) and SINTEX (**d,e,f**) models. For (**a,d**)
1008 precipitation (mm/day), (**b,e**) surface skin temperature (°C) and (**c,f**) Top Of Atmosphere
1009 (TOA) net shortwave radiation (W/m²). In panels (**a**) and (**b**), differences that are above the
1010 95% confidence level according to a permutation procedure with 9999 shuffles are encircled.
1011 In the other panels, the maps only show differences, which are above the 95% confidence
1012 level.

1013

1014 **Figure 7: (a)** Boreal summer (e.g. from June to September) zonal mean precipitation
1015 (mm/day) over an African-Asian domain (70°W-100°E) in the different CFS simulations (see
1016 **Table 2**) against monthly-accumulated precipitation from the Global Precipitation
1017 Climatology Project (Huffman et al. 2009) over the 1979-2010 period, (**b**) as in panel (**a**), but
1018 for the SINTEX simulations (see **Table 2**).

1019

1020 **Figure 8:** Rainfall biases (mm/day) during boreal summer (e.g. from June to September) in
1021 (**a**) ZERO_SINTEX experiment (see **Table 2**) and (**b**) ZERO_CFS experiment (see **Table 2**)
1022 against monthly-accumulated precipitation from the Global Precipitation Climatology Project
1023 (Huffman et al. 2009) over the 1979-2010 period.

1024

1025 **Figure 9:** Boreal summer (e.g. from June to September) differences between the ZERO and
1026 control experiments (see **Table 2**) for CFS (**a,b**) and SINTEX (**c,d**) models. For (**a,c**) 850-
1027 hPa winds (m/s) and Sea Level Pressure (hPa) and (**b,d**) 200-hPa velocity potential (10⁻⁶
1028 m²/s). SLP and 200-hPa velocity potential differences, which are above the 95% confidence
1029 level according to a permutation procedure with 9999 shuffles, are encircled. In panels (**a**)
1030 and (**c**), the maps only show the 850-hPa wind differences, which are above the 95%
1031 confidence level.

1032

1033 **Figure 10:** Improvement or deterioration of simulated tropical rainfall during boreal summer
1034 in the different experiments (e.g. ZERO, MODIS, DESERT) compared to the biases in the
1035 control simulation for each model (e.g. CFS and SINTEX). Following Haywood et al. (2016),
1036 for each model, the improvement/deterioration for ZERO, MODIS and DESERT experiments
1037 with respect to the control simulation is computed as $1 - \text{abs}((\text{EXP}-\text{GPCP})/(\text{CTL}-\text{GPCP}))$,
1038 where EXP is either ZERO, MODIS or DESERT, GPCP is the boreal summer rainfall

1039 climatology for the 1979-2010 period and CTL is the corresponding control simulation. In
1040 this way, positive values represent the percentage improvement in boreal summer rainfall
1041 (and are bounded by 1) and negative values represent the degradation in boreal summer
1042 rainfall compared to the control simulation. **(a)** Boreal summer rainfall improvement or
1043 degradation in ZERO_CFS with respect to CFS, **(b)** Boreal summer rainfall improvement or
1044 degradation in MODIS_CFS with respect to CFS and **(c)** Boreal summer rainfall
1045 improvement or degradation in DESERT_CFS with respect to CFS. **(d)**, **(e)** and **(f)** as **(a)**, **(b)**
1046 and **(c)**, respectively, but for SINTEX model.

1047

1048 **Figure 11:** Boreal summer (e.g. from June to September) differences between the MODIS
1049 and control experiments (see **Table 2**) for CFS **(a,b,c,d)** and SINTEX **(e,f,g,h)** models. For
1050 **(a,e)** albedo (%), **(b,f)** Top Of Atmosphere (TOA) net shortwave radiation (W/m^2), **(c,g)** skin
1051 temperature ($^{\circ}C$) and **(d,h)** sensible heat flux (W/m^2). The maps only show differences,
1052 which are above the 95% confidence level according to a permutation procedure with 9999
1053 shuffles.

1054

1055 **Figure 12:** Surface temperature biases ($^{\circ}C$) during boreal summer (e.g. from June to
1056 September) in **(a)** MODIS_SINTEX experiment (see **Table 2**) and **(b)** MODIS_CFS
1057 experiment (see **Table 2**) against ERA-Interim reanalysis climatology (Dee et al. 2011) over
1058 the 1979-2014 period.

1059

1060 **Figure 13:** Boreal summer (e.g. from June to September) differences between the MODIS
1061 and control experiments (see **Table 2**) for CFS **(a,b,c,d)** and SINTEX **(e,f,g,h)** models. For
1062 **(a,e)** precipitation (mm/day), **(b,f)** 850-hPa winds (m/s) and SLP (hPa), **(c,g)** 200-hPa winds
1063 (m/s) and 200-hPa stream function ($10^{-6} m^2/s$) and **(d,h)** 200-hPa velocity potential (10^{-6}
1064 m^2/s). In panels **(c)** and **(g)**, positive (negative) values of the stream function denote
1065 clockwise (anticlockwise) motions. Precipitation, SLP, 200-hPa stream function and 200-hPa
1066 velocity potential differences, which are above the 95% confidence level according to a
1067 permutation procedure with 9999 shuffles are encircled. In panels **(b)**, **(c)**, **(e)** and **(f)**, the
1068 maps only show the 850 and 200-hPa wind differences, which are above the 95% confidence
1069 level.

1070

1071 **Figure 14:** Boreal summer (e.g. from June to September) differences between the DESERT
1072 and MODIS experiments (see **Table 2**) for CFS **(a,b,c,d)** and SINTEX **(e,f,g,h)** models. For

1073 (a,e) skin temperature ($^{\circ}\text{C}$), (b,f) sensible heat flux (W/m^2), (c,g) precipitation (mm/day) and
1074 (d,h) 850-hPa winds (m/s) and Sea Level Pressure (hPa). In panels (a), (b), (e) and (f), the
1075 maps only show differences, which are above the 95% confidence level according to a
1076 permutation procedure with 9999 shuffles. In panels (c), (d), (g) and (h), precipitation and
1077 SLP differences, which are above the 95% confidence level are encircled and 850-hPa wind
1078 differences are shown only if they are above the 95% confidence level.

1079

1080 **Figure 15:** Rainfall biases (mm/day) during boreal summer (e.g. from June to September) in
1081 (a) DESERT_SINTEX experiment (see **Table 2**) and (b) DESERT_CFS experiment (see
1082 **Table 2**) against monthly-accumulated precipitation from the Global Precipitation
1083 Climatology Project (Huffman et al. 2009) over the 1979-2010 period.

1084

1085 **Figure 16:** (a) Surface temperature bias ($^{\circ}\text{C}$) during boreal summer over the same domain
1086 (land only: latitude 15° - 40°N , longitude 20°W - 75°E) as used in the DESERT experiments for
1087 36 CMIP5 models with respect to surface temperature climatology estimated from ERA-
1088 Interim reanalysis (Dee et al. 2011) over the 1979-2014 period, (b) Rainfall (mm/day)
1089 composite differences between the six warmest and six coldest CMIP5 models over the NH
1090 subtropical deserts, and (c), same as (b), but for SLP (hPa) and 850-hPa winds (m/s)
1091 composite differences. The six CMIP5 models with the highest (lowest) boreal summer land
1092 surface temperature over the NH subtropical deserts (15° - 40°N , 20°W - 75°E) correspond,
1093 respectively, to the CMIP5 models on the extreme right and left of the plot displayed in panel
1094 (a).

1095

1096 **Figure 17:** linear regression between rainfall (mm/day) and the surface temperature ($^{\circ}\text{C}$) over
1097 the NH subtropical desert (15° - 40°N , 20°W - 75°E) in 36 CMIP5 models. Regression
1098 coefficients significant at the 90% confidence level are encircled.

1099

1100
1101

Table Captions

1102 **Table 1:** Description of the 36 Coupled Model Inter-comparison Project phase 5 (CMIP5)
1103 models used in our analysis. We use the historical climate experiments from 36 Coupled
1104 General Circulation Models (CGCMs) contributing to CMIP5 (Taylor et al. 2012; see url:
1105 <http://pcmdi9.llnl.gov>). The 20-year mean during 1980-1999 in historical simulations defines
1106 the present-day climatology. All the diagnostics are performed only for the boreal summer
1107 season (June to September, JJAS hereafter).

1108

1109 **Table 2:** Summary of the coupled ocean-atmosphere experiments performed with the CFSv2
1110 and SINTEX-F2 coupled models. Differences between the coupled simulation configurations
1111 are given in the “Setup” column. The first 10 and 5 years of the simulations for SINTEX and
1112 CFS, respectively, have been excluded from the analyses presented in this study.

1113

1114 **Table 3:** TOA net radiation biases (W/m^2) during boreal summer for the globe and the two
1115 hemispheres in CFS and SINTEX experiments (see **Table 2**) against radiation fluxes
1116 estimates computed from the Clouds and Earth’s Radiant Energy System (CERES) system
1117 (Kato et al. 2013) over the 2000-2014 period.

1118

1119 **Table 4: (a)** Root-Mean-Square-Error (mm/day) for boreal summer rainfall in the different
1120 experiments (see **Table 2**) and different domains against monthly-accumulated precipitation
1121 from the Global Precipitation Climatology Project (Huffman et al. 2009) over the 1979-2010
1122 period. **(b)** Spatial correlation for boreal summer rainfall in the different experiments (see
1123 **Table 2**) and different domains against monthly-accumulated precipitation from the Global
1124 Precipitation Climatology Project (Huffman et al. 2009) over the 1979-2010 period.

1125

1126 **Table 5: (a)** Root-Mean-Square-Error (W/m^2) for boreal summer TOA net radiation, net
1127 shortwave radiation and Outgoing Longwave Radiation (OLR) in the different experiments
1128 (see **Table 2**) for the whole globe against radiation fluxes estimates computed from the
1129 Clouds and Earth’s Radiant Energy System (CERES) system (Kato et al. 2013) over the
1130 2000-2014 period. **(b)** Spatial correlation for boreal summer TOA net radiation, net
1131 shortwave radiation and OLR in the different experiments (see **Table 2**) for the whole globe
1132 against radiation fluxes estimates computed from the Clouds and Earth’s Radiant Energy
1133 System (CERES) system (Kato et al. 2013) over the 2000-2014 period.

Figure 1

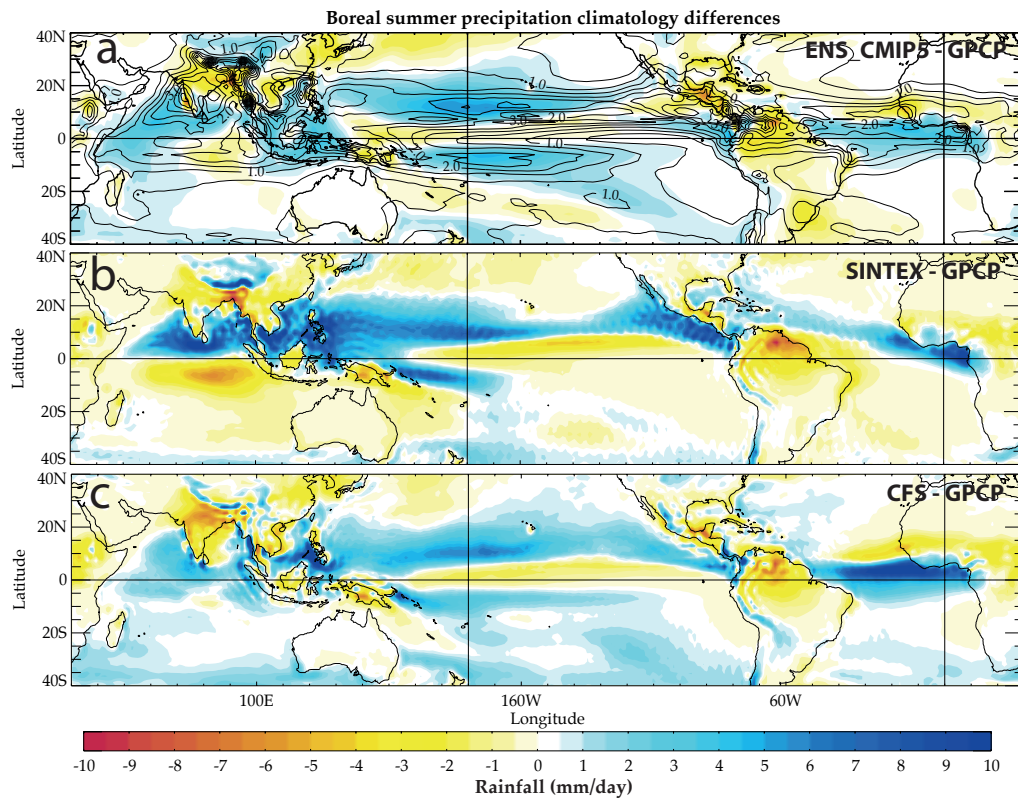


Figure 1: Rainfall biases (mm/day, shading) during boreal summer (e.g. from June to September) in (a) ensemble-mean from 36 CMIP5 CGCMs (see **Table 1**), (b) SINTEX-F2 coupled model (Masson et al. 2012) and (c) Climate Forecast System version2 (CFS) coupled model (Saha et al. 2014) against monthly-accumulated precipitation from the Global Precipitation Climatology Project (Huffman et al. 2009) over the 1979-2010 period. The boreal summer rainfall standard deviation in the 36 CMIP5 CGCMs is also shown as contours (interval every 0.5 mm/day) in panel (a).

Figure 2

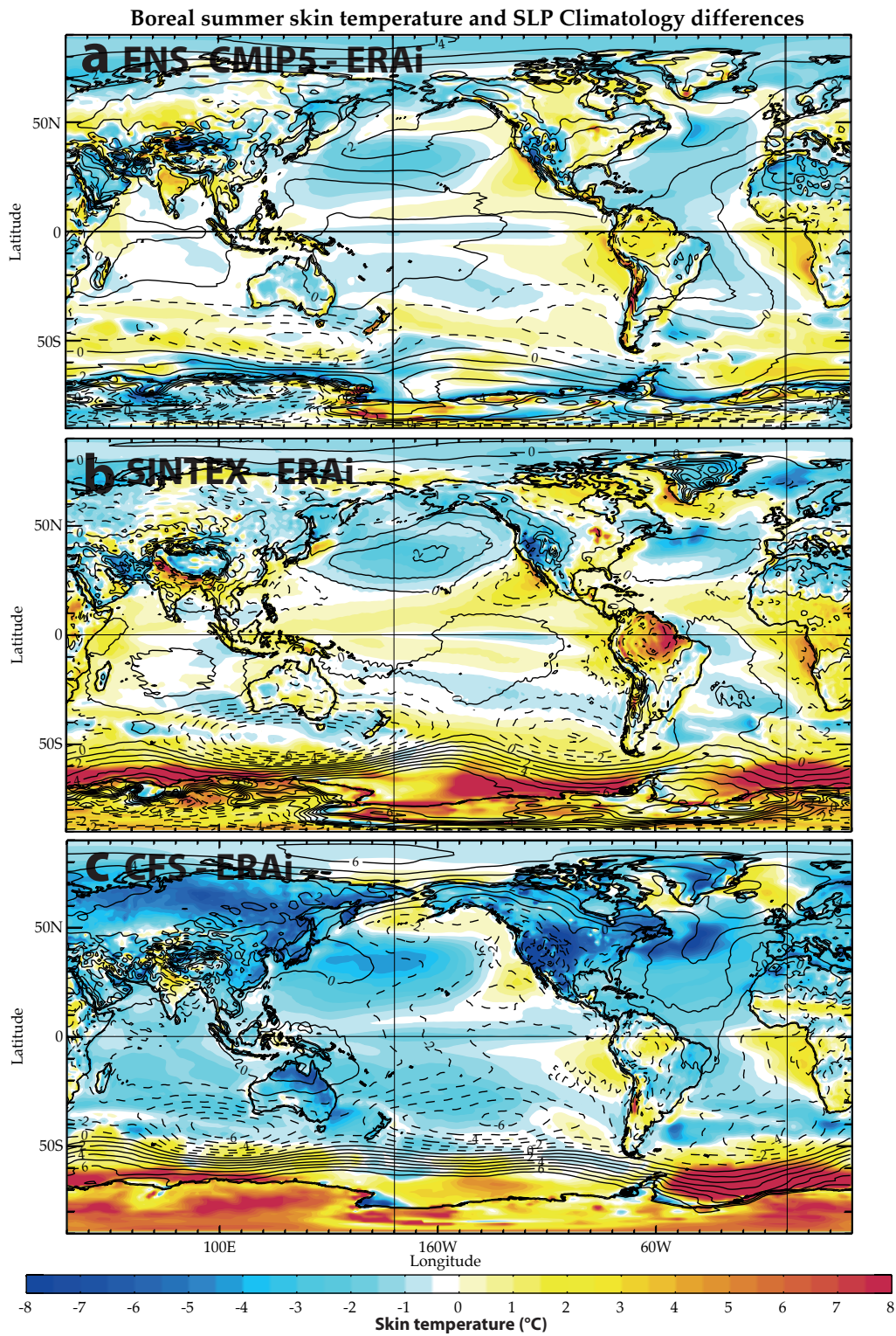


Figure 2: Skin temperature ($^{\circ}\text{C}$, shading) and SLP (hPa, contours every 1-hPa) biases during boreal summer (e.g. from June to September) in (a) ensemble-mean from 36 CMIP5 CGCMs (see Table 1), (b) SINTEX coupled model and (c) CFS coupled model against ERA-Interim reanalysis estimates (Dee et al. 2011) over the 1979-2014 period.

Figure 3

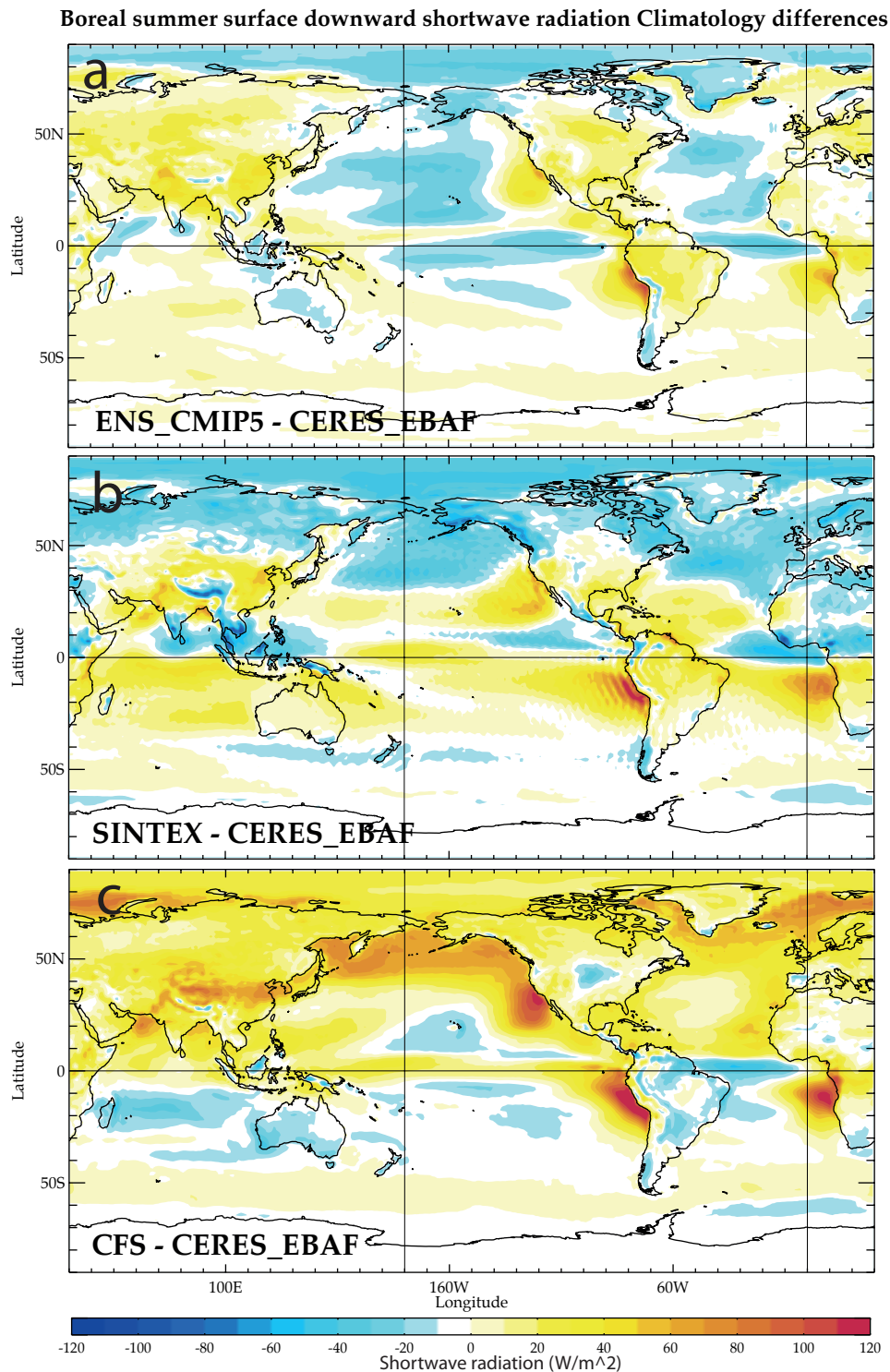


Figure 3: Surface downward shortwave radiation biases (W/m^2) during boreal summer (e.g. from June to September) in (a) ensemble-mean from 36 CMIP5 CGCMs (see **Table 1**), (b) SINTEX and (c) CFS coupled models against estimates from the CERES-EBAF version 2.8 dataset (Kato et al. 2013). The CERES_EBAF boreal summer climatology is estimated from the period 2000-2014.

Figure 4

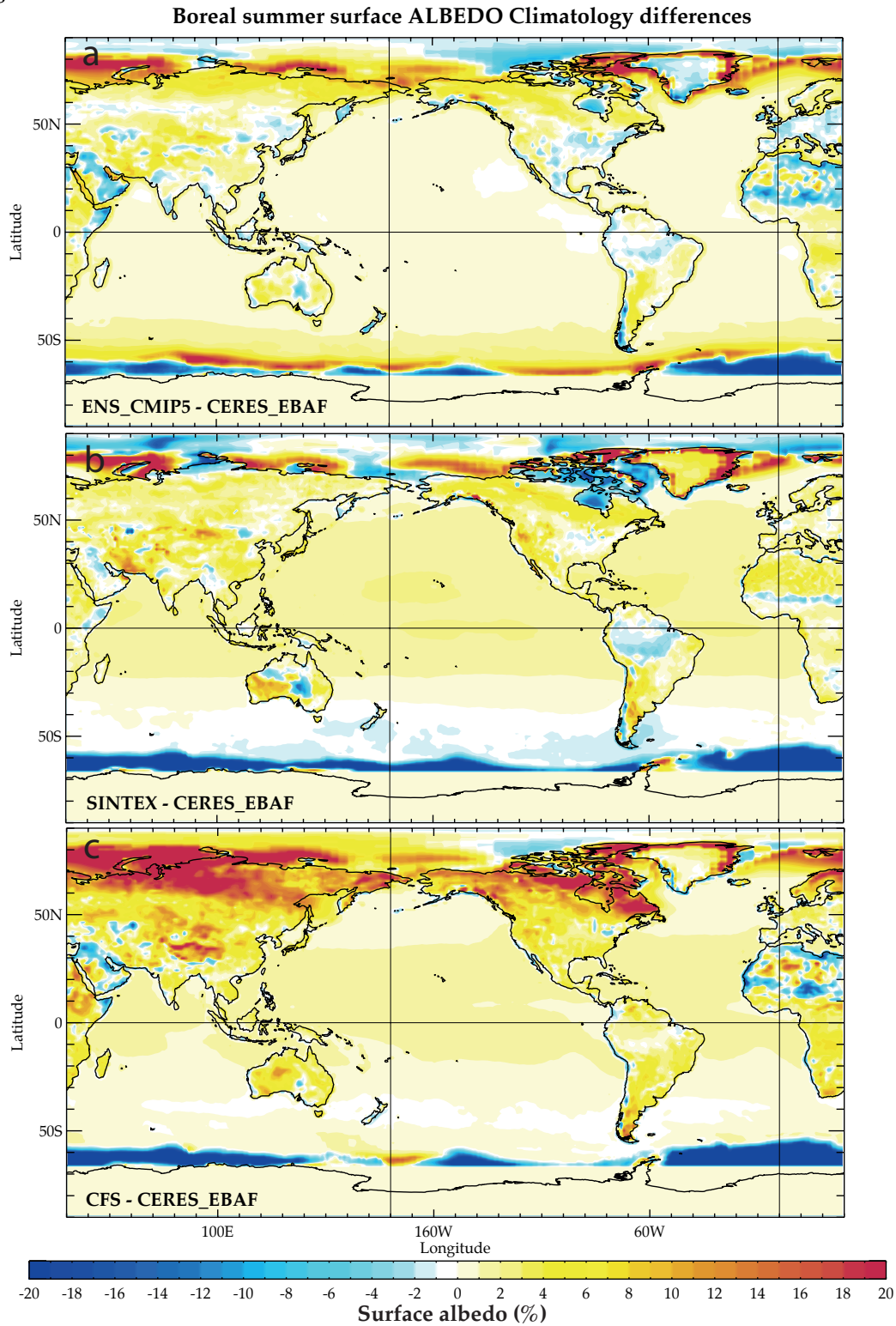


Figure 4: Surface albedo biases (%) during boreal summer (e.g. from June to September) in (a) ensemble-mean from 36 CMIP5 CGCMs (see **Table 1**), (b) SINTEX coupled model and (c) CFS coupled model against radiative fluxes estimates computed from the Clouds and Earth's Radiant Energy System (CERES) system (Kato et al. 2013) over the 2000-2014 period.

Figure 5

Boreal summer snow-free background albedo differences

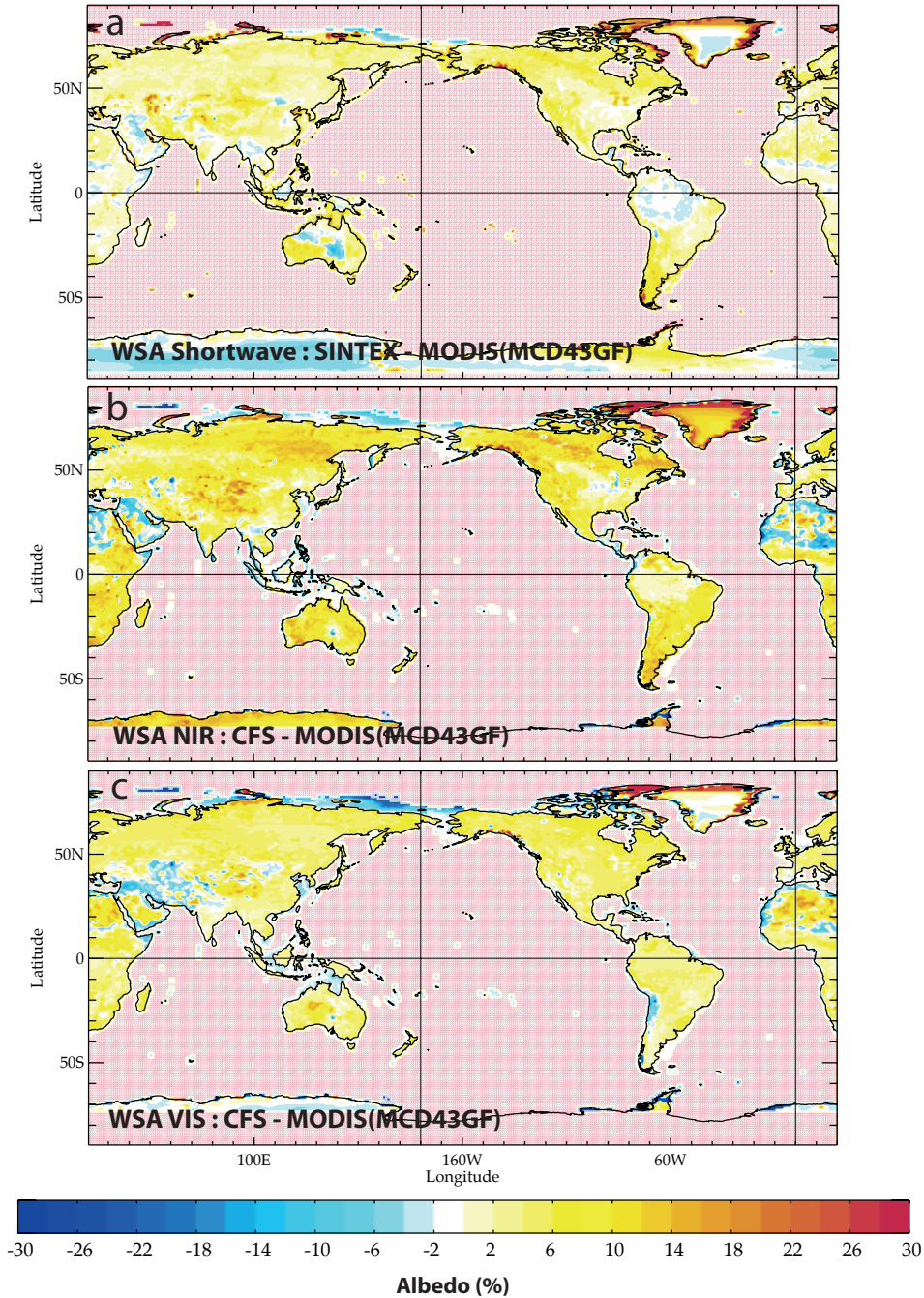


Figure 5: Background snow-free albedo biases (%) over land during boreal summer (e.g. from June to September) for (a) diffuse broadband Short-Wave (SW, 0.3–5.0 μm) albedo in SINTEX CGCM, (b) diffuse Near-Infra-Red (NIR, $>0.7 \mu\text{m}$) albedo in CFS CGCM and (c) diffuse Visible (VIS, $<0.7 \mu\text{m}$) albedo in CFS CGCM against corresponding estimates from the Moderate Resolution Imaging Spectro-radiometer (MODIS) snow-free gap-filled white-sky (diffuse) albedo product MCD43GF-v5 (Schaaf et al. 2011). The MODIS climatologies are estimated from the 2003-2013 period. See Section 2 for further details.

Figure 6

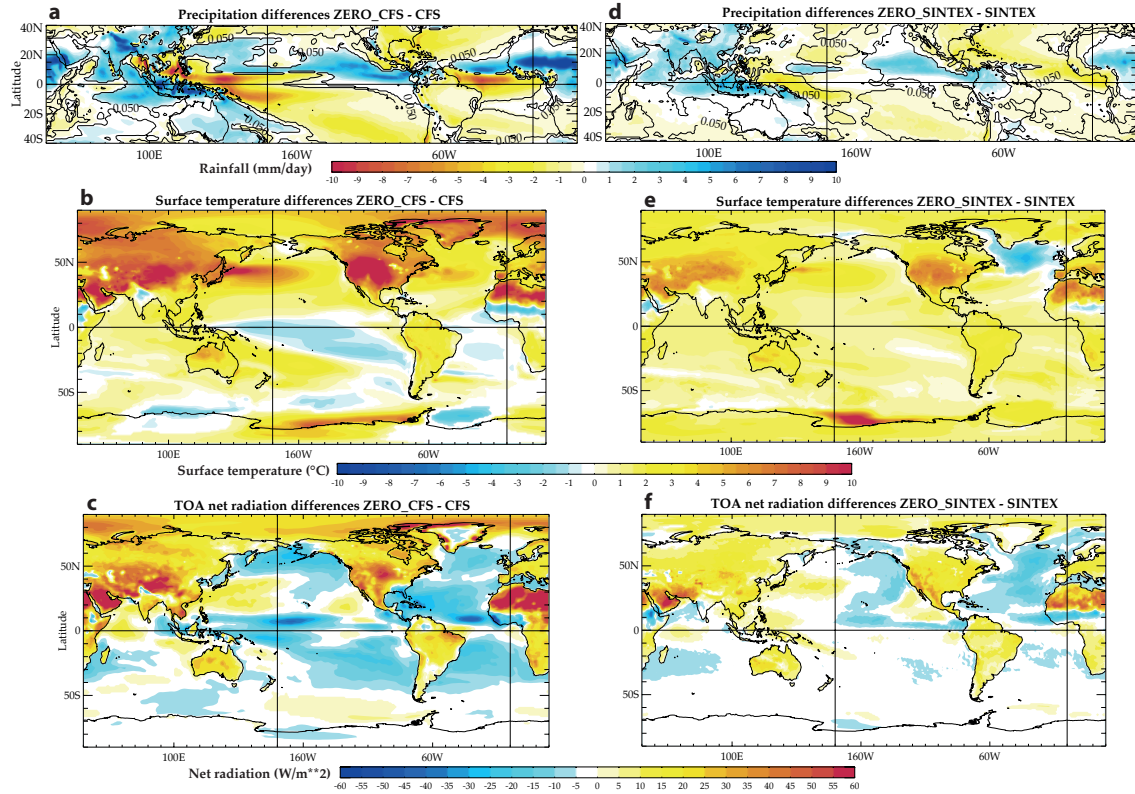


Figure 6: Boreal summer (e.g. from June to September) differences between the ZERO and control experiments (see **Table 2**) for CFS (**a,b,c**) and SINTEX (**d,e,f**) models. For (**a,d**) precipitation (mm/day), (**b,e**) surface skin temperature (°C) and (**c,f**) Top Of Atmosphere (TOA) net shortwave radiation (W/m²). In panels (**a**) and (**b**), differences that are above the 95% confidence level according to a permutation procedure with 9999 shuffles are encircled. In the other panels, the maps only show differences, which are above the 95% confidence level.

Figure 7

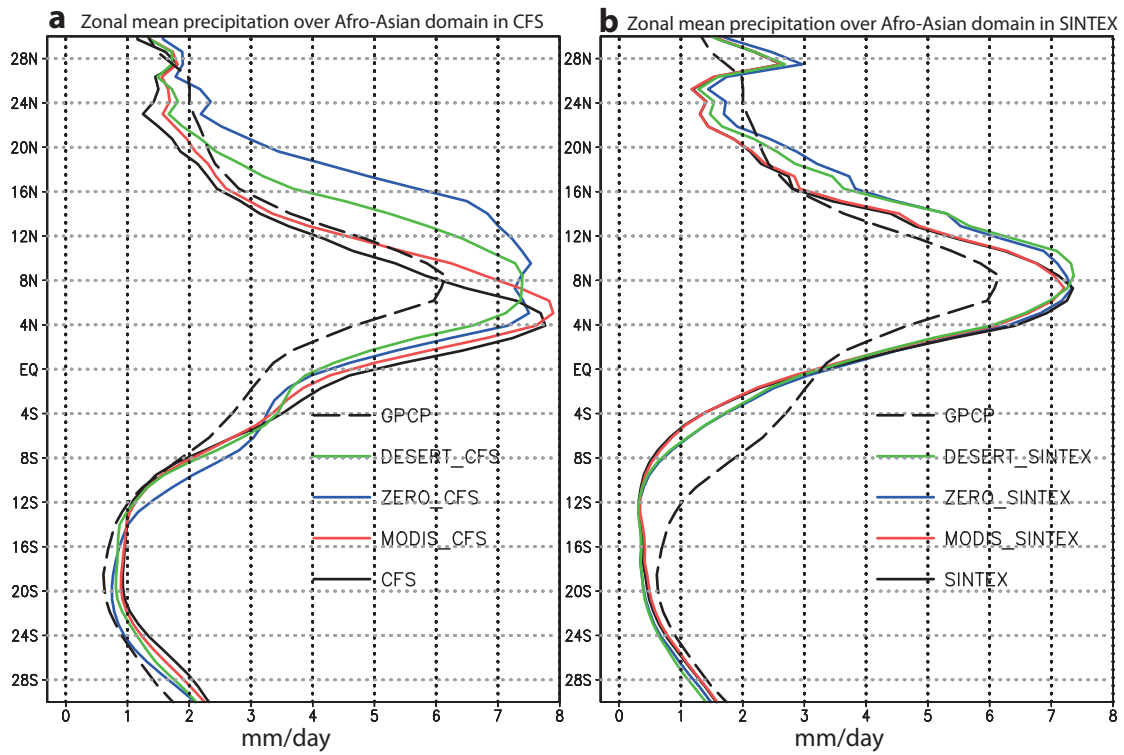


Figure 7: (a) Boreal summer (e.g. from June to September) zonal mean precipitation (mm/day) over an African-Asian domain (70°W-100°E) in the different CFS simulations (see **Table 2**) against monthly-accumulated precipitation from the Global Precipitation Climatology Project (Huffman et al. 2009) over the 1979-2010 period, (b) as in panel (a), but for the SINTEX simulations (see **Table 2**).

Figure 8

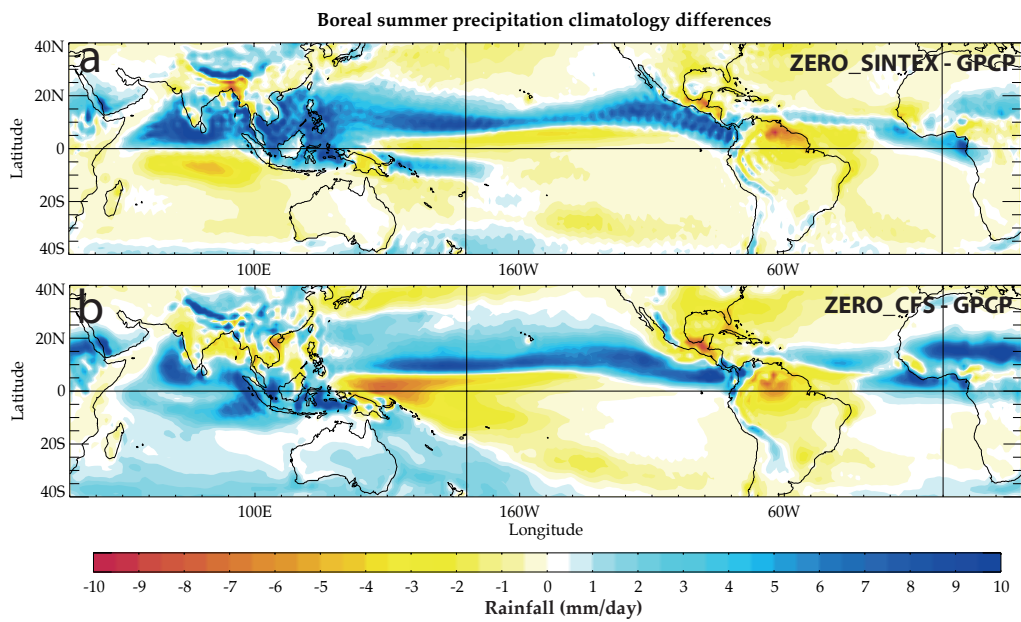


Figure 8: Rainfall biases (mm/day) during boreal summer (e.g. from June to September) in **(a)** ZERO_SINTEX experiment (see **Table 2**) and **(b)** ZERO_CFS experiment (see **Table 2**) against monthly-accumulated precipitation from the Global Precipitation Climatology Project (Huffman et al. 2009) over the 1979-2010 period.

Figure 9

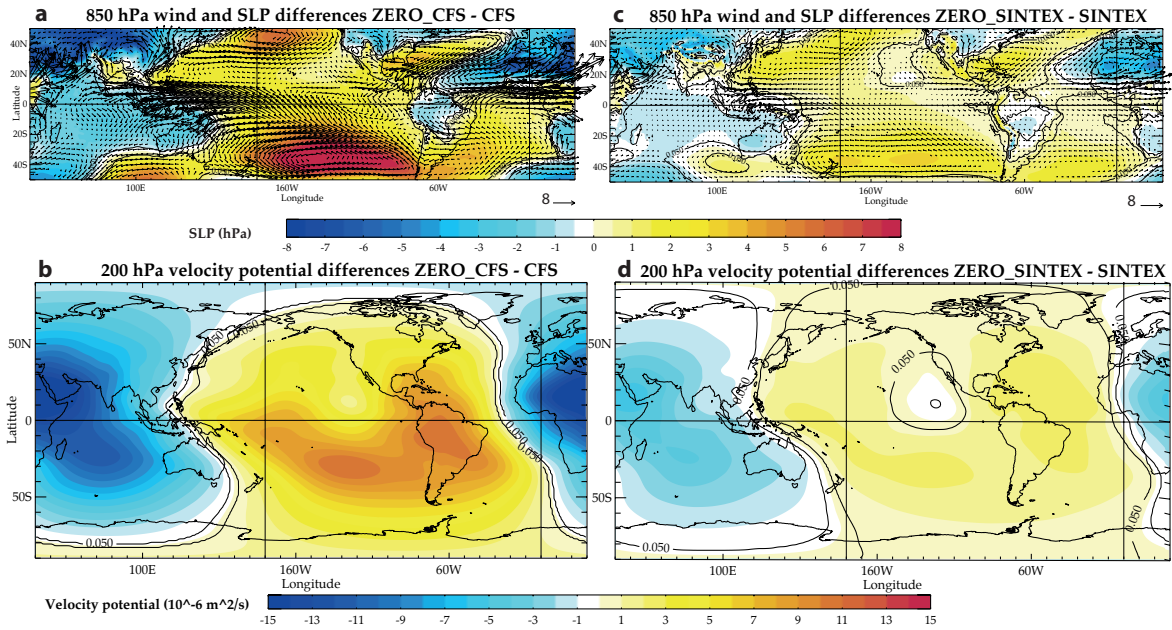


Figure 9: Boreal summer (e.g. from June to September) differences between the ZERO and control experiments (see **Table 2**) for CFS (**a,b**) and SINTEX (**c,d**) models. For (**a,c**) 850-hPa winds (m/s) and Sea Level Pressure (hPa) and (**b,d**) 200-hPa velocity potential ($10^{-6} \text{ m}^2/\text{s}$). SLP and 200-hPa velocity potential differences, which are above the 95% confidence level according to a permutation procedure with 9999 shuffles are encircled. In panels (**a**) and (**c**), the maps only show the 850-hPa wind differences, which are above the 95% confidence level.

Figure 10

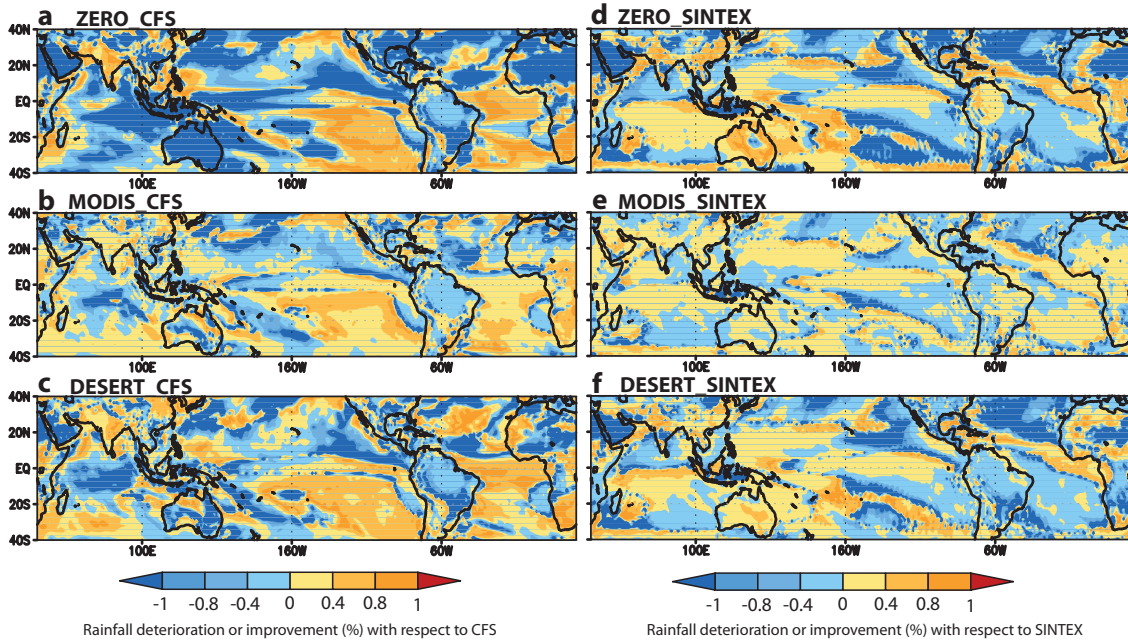


Figure 10: Improvement or deterioration of simulated tropical rainfall during boreal summer in the different experiments (e.g. ZERO, MODIS, DESERT) compared to the biases in the control simulation for each model (e.g. CFS and SINTEX). Following Haywood et al. (2016), for each model, the improvement/deterioration for ZERO, MODIS and DESERT experiments with respect to the control simulation is computed as $1 - \text{abs}((\text{EXP}-\text{GPCP})/(\text{CTL}-\text{GPCP}))$, where EXP is either ZERO, MODIS or DESERT, GPCP is the boreal summer rainfall climatology for the 1979-2010 period and CTL is the corresponding control simulation. In this way, positive values represent the percentage improvement in boreal summer rainfall (and are bounded by 1) and negative values represent the degradation in boreal summer rainfall compared to the control simulation. **(a)** Boreal summer rainfall improvement or degradation in ZERO_CFS with respect to CFS, **(b)** Boreal summer rainfall improvement or degradation in MODIS_CFS with respect to CFS and **(c)** Boreal summer rainfall improvement or degradation in DESERT_CFS with respect to CFS. **(d)**, **(e)** and **(f)** as **(a)**, **(b)** and **(c)**, respectively, but for SINTEX model.

Figure 11

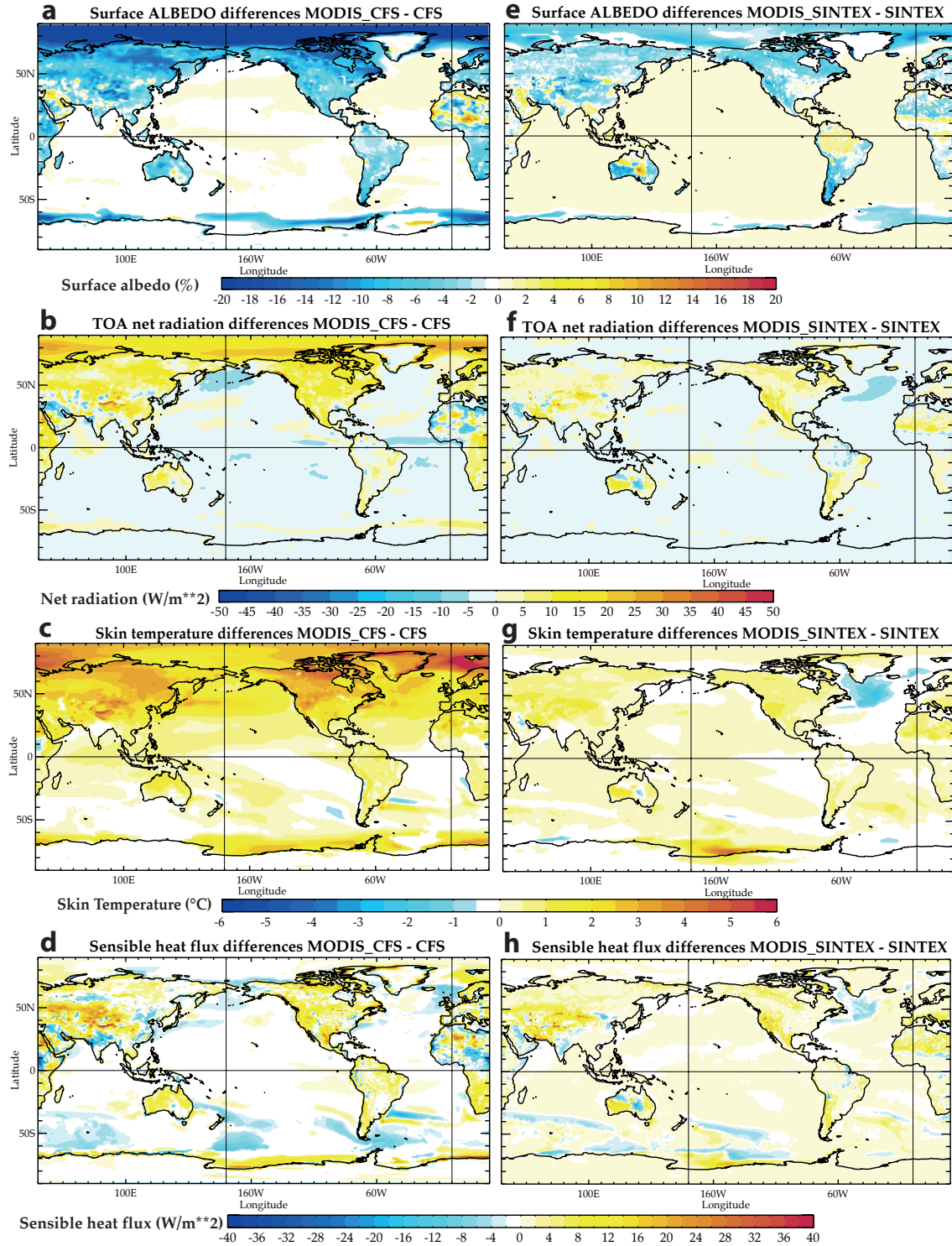


Figure 11: Boreal summer (e.g. from June to September) differences between the MODIS and control experiments (see **Table 2**) for CFS (**a,b,c,d**) and SINTEX (**e,f,g,h**) models. For (**a,e**) albedo (%), (**b,f**) Top Of Atmosphere (TOA) net shortwave radiation (W/m^2), (**c,g**) skin temperature ($^{\circ}C$) and (**d,h**) sensible heat flux (W/m^2). The maps only show differences, which are above the 95% confidence level according to a permutation procedure with 9999 shuffles.

Figure 12

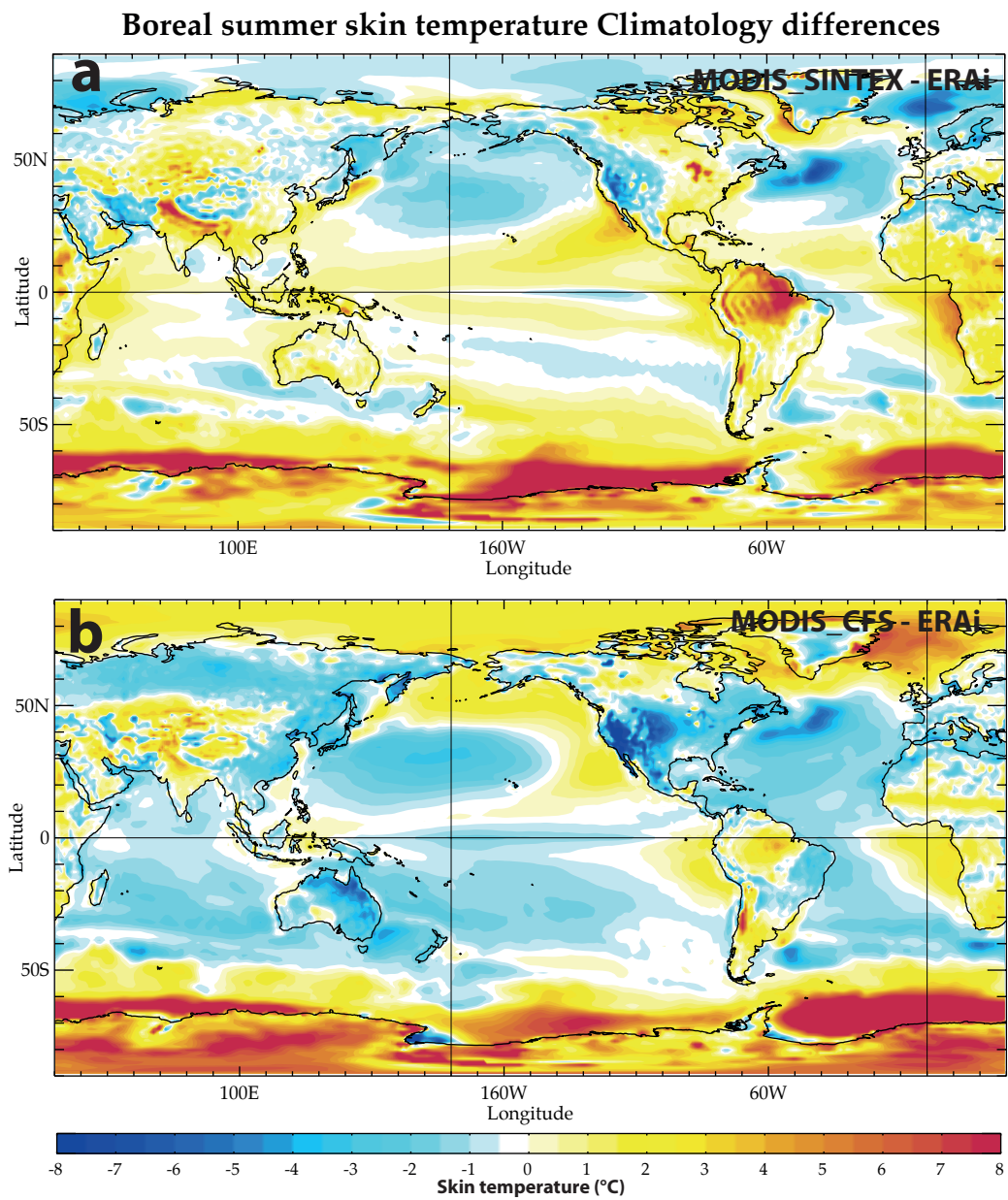


Figure 12: Surface temperature biases ($^{\circ}\text{C}$) during boreal summer (e.g. from June to September) in (a) MODIS_SINTEX experiment (see Table 2) and (b) MODIS_CFS experiment (see Table 2) against ERA-Interim reanalysis climatology (Dee et al. 2011) over the 1979-2014 period.

Figure 13

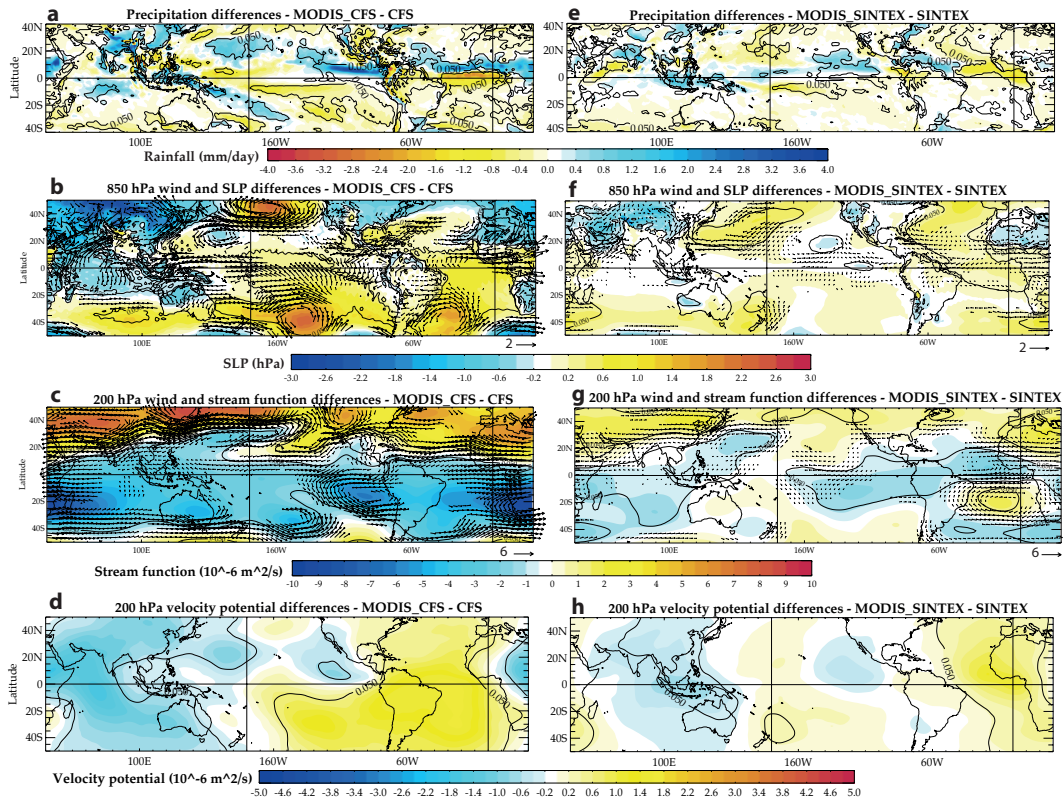


Figure 13: Boreal summer (e.g. from June to September) differences between the MODIS and control experiments (see **Table 2**) for CFS (**a,b,c,d**) and SINTEX (**e,f,g,h**) models. For (**a,e**) precipitation (mm/day), (**b,f**) 850-hPa winds (m/s) and SLP (hPa), (**c,g**) 200-hPa winds (m/s) and 200-hPa stream function ($10^{-6} \text{ m}^2/\text{s}$) and (**d,h**) 200-hPa velocity potential ($10^{-6} \text{ m}^2/\text{s}$). In panels (**c**) and (**g**), positive (negative) values of the stream function denote clockwise (anticlockwise) motions. Precipitation, SLP, 200-hPa stream function and 200-hPa velocity potential differences, which are above the 95% confidence level according to a permutation procedure with 9999 shuffles are encircled. In panels (**b**), (**c**), (**e**) and (**f**), the maps only show the 850 and 200-hPa wind differences, which are above the 95% confidence level.

Figure 14

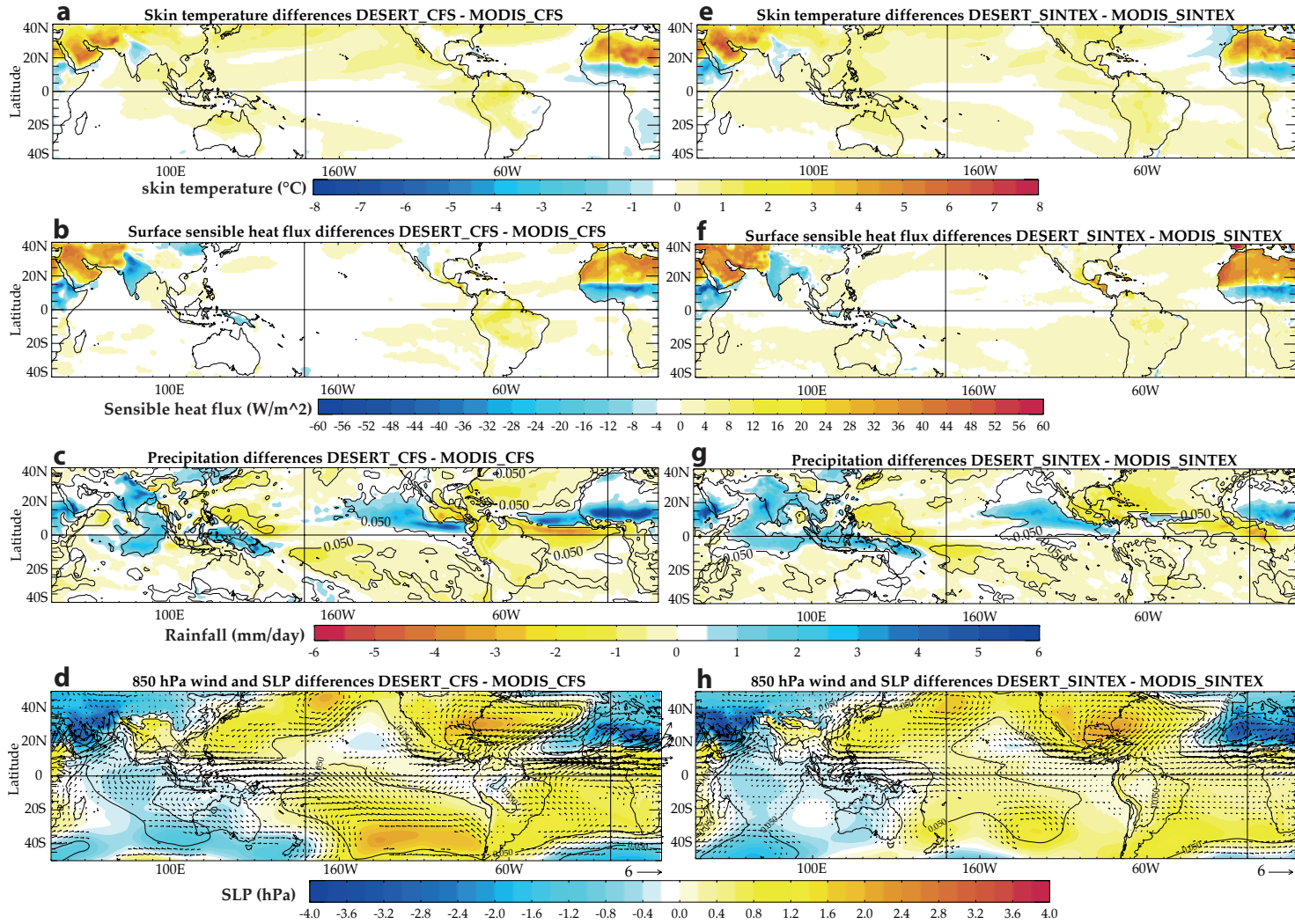


Figure 14: Boreal summer (e.g. from June to September) differences between the DESERT and MODIS experiments (see **Table 2**) for CFS (**a,b,c,d**) and SINTEX (**e,f,g,h**) models. For (**a,e**) skin temperature ($^{\circ}\text{C}$), (**b,f**) sensible heat flux (W/m^2), (**c,g**) precipitation (mm/day) and (**d,h**) 850-hPa winds (m/s) and Sea Level Pressure (hPa). In panels (**a**), (**b**), (**e**) and (**f**), the maps only show differences, which are above the 95% confidence level according to a permutation procedure with 9999 shuffles. In panels (**c**), (**d**), (**g**) and (**h**), precipitation and SLP differences, which are above the 95% confidence level are encircled and 850-hPa wind differences are shown only if they are above the 95% confidence level.

Figure 15

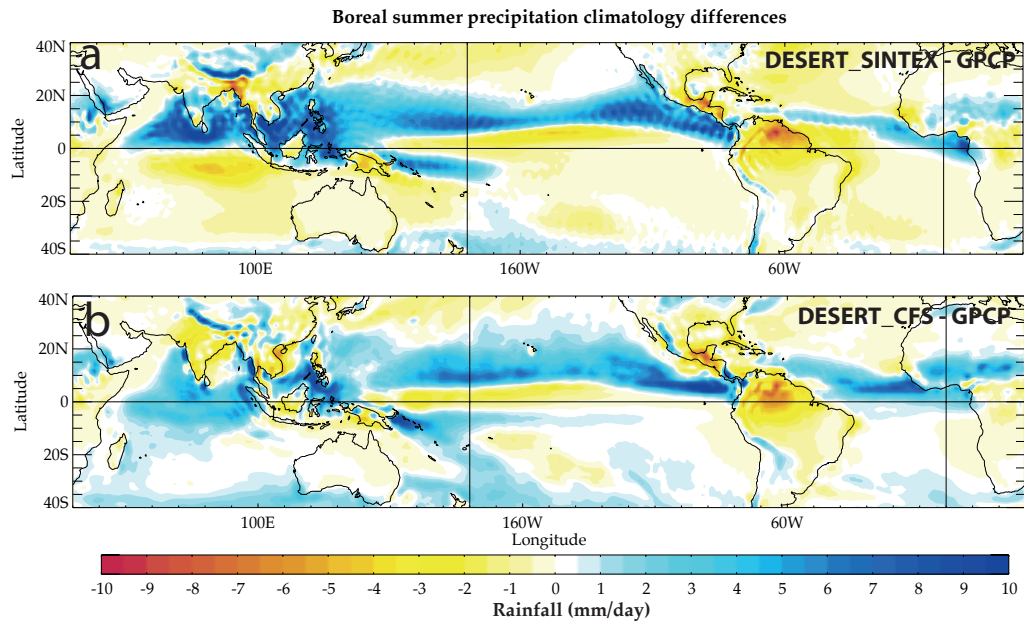


Figure 15: Rainfall biases (mm/day) during boreal summer (e.g. from June to September) in **(a)** DESERT_SINTEX experiment (see **Table 2**) and **(b)** DESERT_CFS experiment (see **Table 2**) against monthly-accumulated precipitation from the Global Precipitation Climatology Project (Huffman et al. 2009) over the 1979-2010 period.

Figure 16

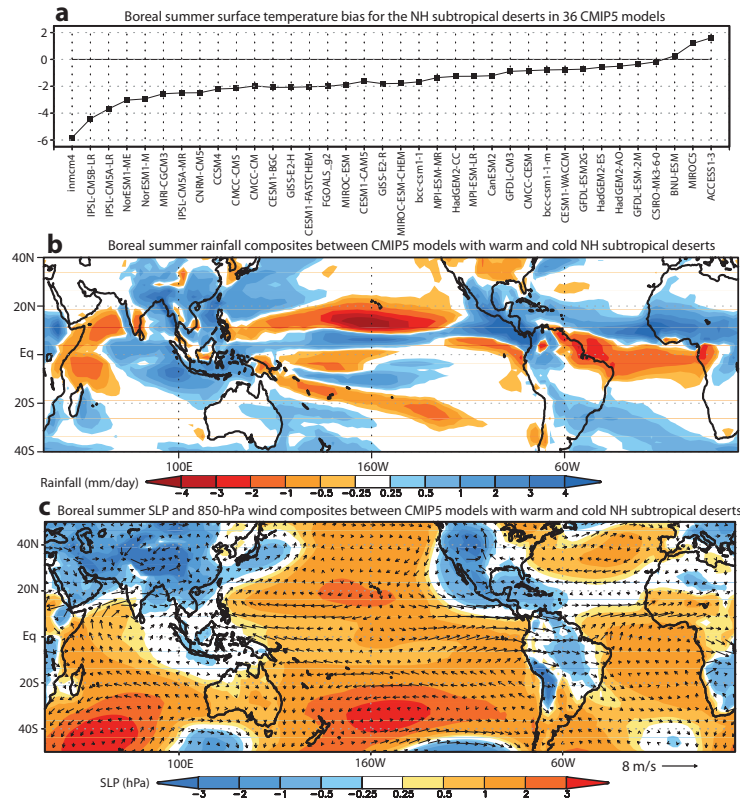


Figure 16: (a) Surface temperature bias ($^{\circ}\text{C}$) during boreal summer over the same domain (land only: latitude 15° - 40°N , longitude 20°W - 75°E) as used in the DESERT experiments for 36 CMIP5 models with respect to surface temperature climatology estimated from ERA-Interim reanalysis (Dee et al. 2011) over the 1979-2014 period, (b) Rainfall (mm/day) composite differences between the six warmest and six coldest CMIP5 models over the NH subtropical deserts, and (c), same as (b), but for SLP (hPa) and 850-hPa winds (m/s) composite differences. The six CMIP5 models with the highest (lowest) boreal summer land surface temperature over the NH subtropical deserts (15° - 40°N , 20°W - 75°E) correspond, respectively, to the CMIP5 models on the extreme right and left of the plot displayed in panel (a).

Figure 17

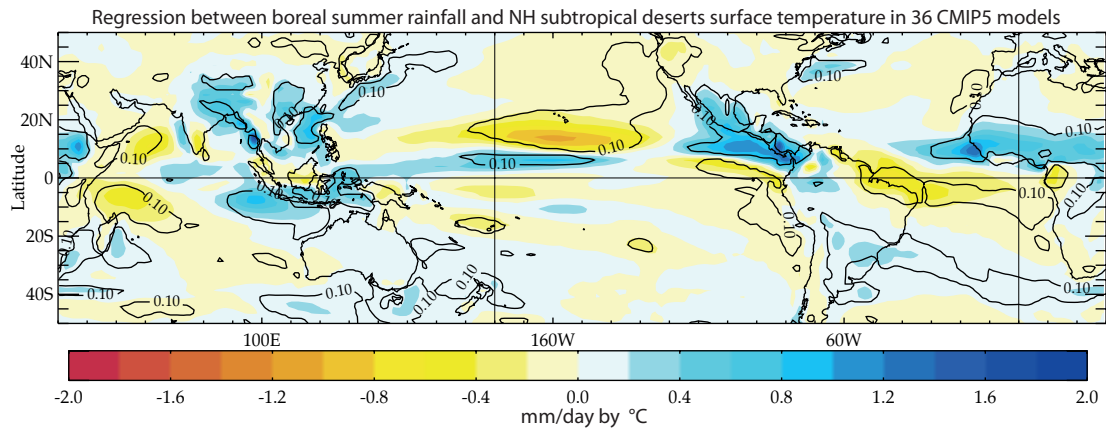


Figure 17: linear regression between rainfall (mm/day) and the surface temperature (°C) over the NH subtropical desert (15°-40°N, 20°W-75°E) in 36 CMIP5 models. Regression coefficients significant at the 90% confidence level are encircled.

No.	Couple model name	Institution	Atmospheric resolution (Lon×Lat, Levels)
1	ACCESS 1.3	Commonwealth Scientific and Industrial Research Organisation and Bureau of Meteorology Australia	192×145, 38
2	BCC-CSM1.1	Beijing Climate Center, China Meteorological Administration	128×64, 26
3	BCC-CSM1.1.m	Beijing Climate Center, China Meteorological Administration	320×160, 26
4	BNU-ESM	Beijing Normal University	128×64, 26
5	CanESM2	Canadian Centre for Climate Modeling and Analysis	128×64, 35
6	CCSM4	National Center for Atmospheric Research	288×192, 26
7	CESM1-BGC	Community Earth System Model Contributors	288×192, 26
8	CESM1-CAM5	Community Earth System Model Contributors	288×192, 26
9	CESM1FASTCHEM	Community Earth System Model Contributors	288×192, 26
10	CESM1-WACCM	Community Earth System Model Contributors	144×96, 66
11	CMCC-CESM	Centro Euro-Mediterraneo sui Cambiamenti Climatici	96×48, 39
12	CMCC-CM	Centro Euro-Mediterraneo sui Cambiamenti Climatici	480×240, 31
13	CMCC-CMS	Centro Euro-Mediterraneo sui Cambiamenti Climatici	192×96, 95
14	CNRM-CM5	Centre National de Recherches Meteorologiques	256×128, 31
15	CSIRO-Mk3.6.0	Commonwealth Scientific and Industrial Research Organisation	192×96, 18
16	FGOALS-g2	Institute of Atmospheric Physics, Chinese Academy of Sciences	128×60, 26
17	GFDL-CM3	Geophysical Fluid Dynamics Laboratory	144×90, 48
18	GFDL-ESM-2G	Geophysical Fluid Dynamics Laboratory	144×90, 48
19	GFDL-ESM-2M	Geophysical Fluid Dynamics Laboratory	144×90, 48
20	GISS-E2-H	NASA Goddard Institute for Space Studies	144×90, 40
21	GISS-E2-R	NASA Goddard Institute for Space Studies	144×90, 40
22	HadGEM2-AO	Met Office Hadley Center, UK	192×145, 38
23	HadGEM2-CC	Met Office Hadley Center, UK	192×145, 60
24	HadGEM2-ES	Met Office Hadley Center, UK	192×145, 38
25	INM-CM4	Institute for Numerical Mathematics	180×120, 21
26	IPSL-CM5A-LR	Institut Pierre-Simon Laplace	96×96, 39
27	IPSL-CM5A-MR	Institut Pierre-Simon Laplace	144×143, 39
28	IPSL-CM5B-LR	Institut Pierre-Simon Laplace	96×96, 39
29	MIROC5	Atmosphere and Ocean Research Institute (The University of Tokyo), and National Institute for Environmental Studies, Japan Agency for Marine-Earth Science and Technology	256×128, 40
30	MIROC-ESM	Japan Agency for Marine-Earth Science and Technology, Atmosphere and Ocean Research Institute (The University of Tokyo), and National Institute for Environmental Studies	128×64, 80
31	MIROC-ESM-CHEM	Japan Agency for Marine-Earth Science and Technology, Atmosphere and Ocean Research Institute (The University of Tokyo), and National Institute for Environmental Studies	128×64, 80
32	MPI-ESM-LR	Max Planck Institute for Meteorology (MPI-M)	192×96, 47
33	MPI-ESM-MR	Max Planck Institute for Meteorology (MPI-M)	192×96, 95
34	MRI-CGCM3	Meteorological Research Institute, Japan	320×160, 48
35	NorESM1-M	Norwegian Climate Centre	144×96, 26
36	NorESM1-ME	Norwegian Climate Centre	144×96, 26

Table 1: Description of the 36 Coupled Model Inter-comparison Project phase 5 (CMIP5) models used in our analysis. We use the historical climate experiments from these 36 Coupled General Circulation Models (CGCMs) contributing to CMIP5 (Taylor et al. 2012; see url: <http://pcmdi9.llnl.gov>). The 20-year mean during 1980-1999 in historical simulations defines the present-day climatology. All the diagnostics are performed only for the boreal summer season (June to September, JJAS hereafter).

Table 2

Acronym	Coupled model	Duration (years)	Setup
SINTEX	SINTEX-F2	210	Control experiment
ZERO_SINTEX	SINTEX-F2	60	Background snow-free broadband shortwave albedo set to zero over land
MODIS_SINTEX	SINTEX-F2	110	Prescribed background snow-free broadband shortwave albedo replaced by MODIS estimates
DESERT_SINTEX	SINTEX-F2	60	Prescribed background snow-free broadband shortwave albedo replaced by MODIS estimates and further decrease by -0.2 over the Sahara, Arabia and Middle-East deserts (land domain: latitude 15°-40°N, longitude 20°W-75°E)
CFS	CFSv2	80	Control experiment
ZERO_CFS	CFSv2	30	Background snow-free diffuse visible and near-infra-red albedo set to zero over land
MODIS_CFS	CFSv2	60	Prescribed background snow-free diffuse visible and near-infra-red albedo replaced by MODIS estimates
DESERT_CFS	CFSv2	30	Prescribed background snow-free diffuse visible and near-infra-red albedo replaced by MODIS estimates and further decrease by -0.2 over the Sahara, Arabia and Middle-East deserts (land domain: latitude 15°-40°N, longitude 20°W-75°E)

Table 2: Summary of the coupled ocean-atmosphere experiments performed with the CFSv2 and SINTEX-F2 coupled models. Differences between the coupled simulation configurations are given in the “Setup” column.

Table 3

Domain	CFS bias	SINTEX bias
Globe	4.6	0.3
NH	8.5	-0.7
SH	0.8	1.2

Table 3: TOA net radiation biases (W/m^2) during boreal summer for the globe and the two hemispheres in CFS and SINTEX experiments (see **Table 2**) against radiation fluxes estimates computed from the Clouds and Earth's Radiant Energy System (CERES) system (Kato et al. 2013) over the 2000-2014 period.

Table 4

Simulation/domain	Tropics (30°S-30°N)	Africa (10°S-20°N, 60°W-40°E)	South Asia (0-25°N, 50°E-100°E)
CFS	2.2	3.2	3.3
ZERO_CFS	2.8	3.5	3.6
MODIS_CFS	2.1	2.3	3.0
DESERT_CFS	2.2	2.3	3.0
SINTEX	2.6	2.4	4.4
ZERO_SINTEX	2.7	1.97	4.8
MODIS_SINTEX	2.5	2	4.2
DESERT_SINTEX	2.5	2.0	4.7

(a) Root-Mean-Square-Error (mm/day) for boreal summer rainfall in the different experiments (see **Table 2**) and different domains against monthly-accumulated precipitation from the Global Precipitation Climatology Project (Huffman et al. 2009) over the 1979-2010 period.

Simulation/domain	Tropics (30°S-30°N)	Africa (10°S-20°N, 60°W-40°E)	South Asia (0-25°N, 50°E-100°E)
CFS	0.83	0.61	0.76
ZERO_CFS	0.76	0.67	0.74
MODIS_CFS	0.86	0.77	0.79
DESERT_CFS	0.86	0.87	0.84
SINTEX	0.82	0.77	0.67
ZERO_SINTEX	0.83	0.80	0.71
MODIS_SINTEX	0.84	0.81	0.7
DESERT_SINTEX	0.84	0.82	0.8

(b) Spatial correlation for boreal summer rainfall in the different experiments (see **Table 2**) and different domains against monthly-accumulated precipitation from the Global Precipitation Climatology Project (Huffman et al. 2009) over the 1979-2010 period.

Table 5

Simulation/variable	TOA net radiation	TOA net shortwave radiation	OLR
CFS	18.5	18.2	10.6
ZERO_CFS	25	25.1	14.2
MODIS_CFS	18.5	18.6	9.3
DESERT_CFS	21.1	20.1	10.1
SINTEX	13.3	16.1	10.1
ZERO_SINTEX	15.9	17.8	10.1
MODIS_SINTEX	13.5	15.9	9.7
DESERT_SINTEX	17.6	18.4	10.8

(a) Root-Mean-Square-Error (W/m^2) for boreal summer TOA net radiation, net shortwave radiation and Outgoing Longwave Radiation (OLR) in the different experiments (see **Table 2**) for the whole globe against radiation fluxes estimates computed from the Clouds and Earth's Radiant Energy System (CERES) system (Kato et al. 2013) over the 2000-2014 period.

Simulation/variable	TOA net radiation	TOA net shortwave radiation	OLR
CFS	0.97	0.98	0.95
ZERO_CFS	0.95	0.97	0.91
MODIS_CFS	0.98	0.98	0.97
DESERT_CFS	0.97	0.98	0.96
SINTEX	0.98	0.98	0.96
ZERO_SINTEX	0.98	0.98	0.96
MODIS_SINTEX	0.98	0.99	0.96
DESERT_SINTEX	0.97	0.98	0.95

(b) Spatial correlation for boreal summer TOA net radiation, net shortwave radiation and OLR in the different experiments (see **Table 2**) for the whole globe against radiation fluxes estimates computed from the Clouds and Earth's Radiant Energy System (CERES) system (Kato et al. 2013) over the 2000-2014 period.